Check for updates

Polymer Composites

WILEY | spe INSPIRING PLASTICS PROFESSIONALS

RESEARCH ARTICLE OPEN ACCESS

Combined Effects of Thermal Cycling Aging and Reinforcement Content on the Ball-On-Disk Wear of Additively Manufactured Polylactic Acid Composites

Sinan Fidan[1] | Satılmış Ürgün[2] | Nevin Gamze Karsli[3] | Taner Yilmaz[4] | Mustafa Özgür Bora[1] | Mehmet İskender Özsoy[5]

[1]Department of Airframe and Powerplant Maintenance, Faculty of Aeronautics and Astronautics, Kocaeli University, Kocaeli, Türkiye | [2]Department of Aviation Electrics and Electronics, Faculty of Aeronautics and Astronautics, Kocaeli University, Kocaeli, Türkiye | [3]Department of Aerospace Engineering, Faculty of Aeronautics and Astronautics, Kocaeli University, Kocaeli, Türkiye | [4]Department of Mechanical Engineering, Engineering Faculty, Kocaeli University, Kocaeli, Türkiye | [5]Department of Mechanical Engineering, Faculty of Engineering, Sakarya University, Sakarya, Türkiye

Correspondence: Mehmet İskender Özsoy (iozsoy@sakarya.edu.tr)

Received: 18 July 2026 | **Revised:** 5 August 2026 | **Accepted:** 7 August 2026

Keywords: additive manufacturing | ball-on-disk wear | polylactic acid composites | thermal cycling aging

ABSTRACT

This study focuses on the additive manufacturing of pure polylactic acid (PLA) specimens and milled glass fiber (GF)-filled PLA composites under thermal cycling aging and wear tests. Wear tracks have been analyzed via 3D optical profiling and SEM imaging. DSC was used to characterize the material changes caused by thermal cycling rather than to determine friction-induced heating or thermal softening during the wear tests. Factorial ANOVA has been used to evaluate the contribution of different factors. Reinforcement of PLA decreased wear depth in case of 50 mm s^{-1} sliding speed in all aging cases; 15 wt% GF lowered wear depth to 81 μm from 217 μm for pure PLA after 400 aging cycles. Under maximum aging and sliding speed of 100 mm s^{-1}, wear resistance has been degraded due to the degradation of interface and fiber pull-out that promoted the third body abrasive wear; hence aged 10 wt% GF composite was the most worn specimen. ANOVA found material composition as the main factor affecting wear depth (34.67%), while interaction factors affected friction coefficient (61.54%).

1 | Introduction

Because of the capability of additive manufacturing (AM) to produce complex geometries, it has garnered immense attention in several fields like the automotive industry, aerospace, and biomedicine [1–3]. Polylactic acid (PLA) is one of many thermoplastics used in AM, which has been valued because of its superior processability, biodegradability, and environmental friendliness [4, 5]. However, there are some limitations associated with pure PLA, such as thermal instability, brittleness, and poor tribology [6, 7].

A number of studies have been done on the key role of post-printing secondary operations in improving the mechanical properties of composite elements by influencing their internal structure and interlayers interaction, thus increasing the mechanical, physical, and surface properties of composite materials [8–11]. Nassar et al. [8] conducted research on the effect of infill percentage, geometric internal design and heat treatment on the mechanical properties of carbon fiber (CF) reinforced PLA composites. The authors found out that the elastic modulus of composites does not depend on the production process or thermal structuring process while the ultimate tensile strength and surface hardness are determined by the kind of raw material used and the degree of internal fillings. Besides, high temperatures cause molecular-level melting and removal of internal voids and prevent brittle fracture, thus providing cohesive adhesion mechanisms. Bolat et al. [9] evaluated the mechanical properties

This is an open access article under the terms of the Creative Commons Attribution-NonCommercial-NoDerivs License, which permits use and distribution in any medium, provided the original work is properly cited, the use is non-commercial and no modifications or adaptations are made.

© 2026 The Author(s). *Polymer Composites* published by Wiley Periodicals LLC on behalf of Society of Plastics Engineers.

Highlights

- Thermal cycling aging severely degrades wear resistance of FDM-printed PLA.
- 15 wt% GF limits wear depth to 81 μm after 400 cycles versus 217 μm for pure PLA at 50 mm/s.
- High speed plus maximum aging inverts the reinforcement hierarchy via third-body abrasion.
- Aged 10 wt% GF composite shows the deepest wear scar (209 μm; Sz = 716.5 μm) at 100 mm/s.
- ANOVA; material dominates wear depth (34.67%); interactions govern friction (61.54%).

and surface smoothness of acrylonitrile styrene acrylate (ASA) products created through AM with acetone vapor treatment, experimentally varied layer height, infill ratio and exposure time and applied optimization models based on machine learning and deep learning approaches. The maximum product hardness was recorded for 100% infill with 45 min of acetone exposure and excessive exposure resulted in material softening. The highest result for surface smoothness was obtained with processing time equal to 90 min. Similarly, in another study, Bolat et al. [10] investigated the influence of layer thicknesses and postproduction baking and liquid impregnation on tensile and impact characteristics of PLA, acrylonitrile butadiene styrene (ABS), and polyethylene terephthalate glycol (PETG) polymer materials produced through AM. According to the study, the effect of heat was positively correlated with tensile and impact characteristics of materials. Nevertheless, the extraction of moisture from the products contributed to their higher elongation at break because of weight increase. Decreasing the layer thickness had a positive effect on tensile characteristics but decreased impact force. Kočiško et al. [11] studied how postproduction processing techniques such as sandblasting and grinding improve the surface quality of PLA and metal powder composites (iron, steel, bronze) manufactured through AM. It was found out that sandblasting with silica sand reduced surface roughness by 80% to 90%. Products that were printed quickly by means of relatively thick layers had a smoother profile than those without post-processing operations with thin layers. After that, a stepped grinding process was used to get the surface finish in sub-micron range, thus achieving mirror-like shine of steel and PLA composites.

On the other hand, many researchers have studied the addition of different fillers and reinforcements into PLA to improve mechanical, thermal, and tribological properties; for example, Ahmed et al. [12] created different layered sandwich structures with various reinforcement ratios of PLA and CF-reinforced PLA composites through AM technology. The research covered such parameters as mechanical, thermal, and microstructural analysis by means of tensile, compression, bending, and stiffness testing and thermal analysis and microstructural characterization. High reinforcement ratios provided an improvement in tensile strength and stiffness, while medium reinforcement ratios gave the optimal flexibility. Low reinforcement ratios were beneficial under compressive conditions. Also, the use of CF improved the thermal stability and increased the degradation temperatures. Jagadeesh et al. [13] synthesized PLA composites with 2–6 wt% wollastonite filler through AM process and investigated how the geometry of filler due to AM process affects the mechanical properties of PLA. These specimens were tested on tensile, bending, impact, and hardness. The results revealed that increasing filler content usually leads to better strength and stiffness. In the case of high filler content, the distribution of particles in the matrix is mostly homogeneous, and the interfacial bonding was responsible for improving the mechanical properties. Ozah et al. [14] manufactured AM-printed PLA composites with silicon nitride particles. According to the research findings, the samples with 1 vol% fillers and 75 wt% infill provided peak mechanical properties like impact resistance, hardness, flexural strength, and tensile strength because of the homogeneous distribution of particles in the matrix. On the other hand, high infill volume with a 2 vol% filler ratio reduced wear losses and friction coefficient and gave the best results concerning thermal stability and flame retardancy.

Vishal et al. [15] investigated the influence of the changing level of silicon filler addition on PLA. A concentration of silicon at 5% led to improvement in all tested mechanical properties of PLA, namely its hardness, tensile, bending, impact, and compressive strength. At the same time, this filler created a protective layer on the friction surface, significantly reducing both wear and coefficient of friction (COF). An increase in filler content to 7%, however, resulted in weakening of the structure of the filament. Abed et al. [16] studied wear characteristics of PLA and CF + PLA composites obtained through the AM process. Test samples were tested for their wear performance in dry sliding conditions for different loads, and the analysis of data was conducted using statistical optimization methods. It was revealed that the ratio of fillers is the key characteristic for wear performance, while the load is less influential. The higher content of fillers provides greater ability of materials to resist friction. Lasch et al. [17] studied tribological properties of pure PLA, pure TPU, and bronze-reinforced PLA printed through the AM process. Although the highest hardness was found for pure PLA, the highest wear was found for the samples of pure PLA because of lack of capability to create a protective layer.

Kaplan [18] made a comparative evaluation of the wear performance of pure PLA composites filled with tungsten particles, prepared by AM, subjected to various loads and sliding distances using the pin-on-disk testing technique. The study revealed that wear rose with increasing load and sliding distance for the materials used; however, the introduction of tungsten increased the wear resistance of PLA, especially under low and moderate loads. Loss of material showed to be less in case of reinforced composites, and the specific wear rate had a more consistent tendency. Tyagi et al. [19] produced PLA composites printed through AM with molybdenum disulfide (MoS_2) and silicon carbide (SiC) fillers and determined the effect of various parameters of filament preparation and printing on tribological and surface characteristics like wear, friction, surface roughness, morphology, and wettability. The presence of MoS_2 and SiC considerably increased the wear resistance of the PLA matrix, improved the friction performance, and increased the surface energy. Selwin et al. [20] added 20 wt% microcrystalline cellulose to AM-based PLA and studied the mechanical and wear performance of the composite thus obtained. Improvement was found in terms of tensile, flexural, impact, and compressive strength in

15480569, 0, Downloaded from https://4spepublications.onlinelibrary.wiley.com/doi/10.1002/pc.71528 by Turkey Cochrane Evidence Aid, Wiley Online Library on [14/08/2026]. See the Terms and Conditions (https://onlinelibrary.wiley.com/terms-and-conditions) on Wiley Online Library for rules of use; OA articles are governed by the applicable Creative Commons License

comparison with pure polymer. Furthermore, wear parameter values such as sliding speed, sliding distance, and loading were considered using ANOVA for COF and wear volume.

The properties of composite parts depend not only on the reinforcement material and amount of the reinforcement used but also on environmental factors, which are especially important when considering aerospace engineering. In this case, cyclic changes of temperature play a decisive role in determining the behavior of materials in the long run. Cyclic changes of temperature contribute to accumulation of thermally induced residual stresses at the interface between the matrix and the reinforcement because of different coefficients of thermal expansion (CTE) [21, 22]. Thermal cycling can cause matrix embrittlement, degradation of interphase interaction, micro-cracking, and changes of surface integrity of the composites [23–25]. At the same time, additive-manufactured samples may demonstrate increased sensitivity to thermal cycling because of anisotropy resulting from the peculiarities of the production process [26]. Xu et al. [27] investigated the effect of accelerated aging on PLA/polyhydroxyalkanoate (PHA) blended additive-manufactured samples. After exposing the samples to aging of different duration, such characteristics as the degree of color changes, chemical structure, thermal properties, rheology, mechanical performance in tensile and flexural tests, and fracture morphology were analyzed. According to the research results, during the initial stage of aging, mechanical performance did not improve because of chain rearrangement and increase of the fraction of crystallinity; however, in the course of time, the effects of degradation prevail, resulting in reduction of strength and stiffness. Furthermore, prolonged aging leads to such changes as color changes, deterioration of molecular structure, and decrease of adhesion between layers of the material. Khosravani and Reinicke [28] estimated the effect of repeated temperature changes on tensile behavior of PLA additive-manufactured samples. After exposing the samples to temperature cycles below the glass transition temperature for 2 weeks, tensile testing demonstrated no changes of size and mass; however, the maximum value of the load was reduced, showing that environmental exposure negatively affects the mechanical performance of the sample.

In addition to scientific value, the current research carries practical significance and presents practical industrial applications. For example, material-extrusion-based AM of PLA and PLA/GF composites has become a more and more popular technique to fabricate not just prototypes but functional and load-bearing end-use parts. Specific examples are bushings, bearing cages, gears, guide rails, hinges, latches, snap-fit joints, brackets for drone and unmanned aerial vehicle (UAV) airframes, protective housing for outdoor sensors and telecommunication equipment, as well as custom jig and fixtures and robotic end effectors working in sliding contact with metallic parts. However, in operation, such parts are not exposed to ideal laboratory conditions, but rather operate in the presence of diurnal and seasonal temperature changes with high humidity, condensation and frost-thaw cycles. Such environmental exposure is simulated in the current study with IEC 60068-3-5 cycling protocol. Therefore, the experimental results present engineers with practically useful, quantitative guidelines: the composition of an FDM-printed tribological part cannot be chosen based on data sheets collected in perfect conditions, because the ranking of wear resistance of different material grades could either be conserved (e.g., 15 wt% GF material limits wear to 81 vs. 217 μm for pure PLA at 50 mm/s even after 400 cycles) or totally inverted (after aging, 10 wt% GF material becomes the poorest performer at 100 mm/s). Practically speaking, the methodology proposed in the current paper (combined thermal cycling and ball-on-disk tests) could become a low-cost method of qualification of additively manufactured parts in the aerospace, automotive, marine, and outdoor infrastructure industry sectors. Factorial ANOVA contributions provided by the current research can be used for lifetime predictions and planning of maintenance of printed polymer components and material selection in digital tools. Finally, through establishing the range of environmentally friendly application conditions of a biodegradable, biopolymer composite, the current research contributes to industrial transition toward sustainable on-demand manufacturing of spare parts.

However, the design of these elements still lacks a scientifically incomplete foundation, which highlights the need for the study in question. The available literature shows that the durability of additively manufactured PLA-based composites has so far been studied in terms of two separate research lines, uncoupled from each other: one research line quantifies the effect of the reinforcement type and amount on the friction and wear in the pristine, as-printed condition, whereas another investigates the thermal stability and mechanical integrity during the process of thermal cycling and aging without the wear assessment. But when considering a specific component, this split represents a real design challenge. Consider a printed PLA/GF bushing supporting the rotating steel shaft of an agricultural field robot, a worm gear of the pan-tilt drive of a highway surveillance camera, a bracket of the servo control horn sliding against the steel pin of a UAV wing, which is exposed to sub-zero temperatures after the summertime heating on the ground, or a snap-fit hinge of a roadside enclosure for sensors undergoing nightly dew and frost; all of these metal-polymer sliding pairs go through hundreds of thermo-hygrometric cycles before reaching their wear life. In this case, the designer faces a question that cannot be answered within either of the above-mentioned research lines: does a certain amount of glass fibers (GFs) continue to provide the sliding surface protection after thermal cycles and aging in humidity environment, or, on the contrary, the degraded fiber–matrix interface turns the reinforcement into a material damaging the surface in form of the third body. As far as known, no research has yet investigated how the interplay between the aging due to the thermal cycling and the amount of reinforcement affects the wear behavior of additively manufactured PLA composites. The investigation of this interplay is critical for understanding the degradation mechanism, which in turn determines the efficiency of the reinforcement under service conditions. Therefore, the novelty of the current research is the first systematic, full-factorial quantification of the mentioned interplay: Pure PLA and PLA composites containing 10 and 15 wt% of milled GFs underwent 0, 200, and 400 thermo-hygrometric cycles in accordance with the standard IEC 60068-3-5 and were tested against the 100Cr6 steel using the ball-on-disk test setup at two sliding speeds. Based on the results of 3D optical profilometry, SEM, DSC and factorial ANOVA analyses, it has been found that the protection

15480569, 0, Downloaded from https://4spepublications.onlinelibrary.wiley.com/doi/10.1002/pc.71528 by Turkey Cochrane Evidence Aid, Wiley Online Library on [14/08/2026]. See the Terms and Conditions (https://onlinelibrary.wiley.com/terms-and-conditions) on Wiley Online Library for rules of use; OA articles are governed by the applicable Creative Commons License

ranking of the reinforcement is not an intrinsic property of the materials but rather a regime-dependent phenomenon, which can be entirely inverted by the combined effect of aging and sliding speed.

2 | Materials and Methods

2.1 | Filament Fabrication Process

The research used PLA polymer matrix, which is commercially available under Ingeo Biopolymer 4043D by NatureWorks. Properties of Ingeo 4043D, according to the manufacturer, are as follows: melt flow index at 210°C and with a load of 2.16 kgf equal to 6 g/10 min, relative viscosity in 1% chloroform solution, ASTM D5225 equal to 4.0, and density ASTM D792 equal to 1.24 g/cm^3. GF Omfil (milled) was chosen as a reinforcing material for filaments with a diameter of about 13 μm and a length of 200 μm. To avoid any moisture influence on the processing process, PLA and milled GF were dried in a vacuum oven at a temperature of 80°C for 4 h before the manufacturing process started. After drying, three formulations for the filament production were made: PLA, PLA with 10% of GF, and PLA with 15% of GF.

These filaments were made through three different sample preparation procedures, using an extruder provided by Kökbir (Kökbir İthalat İhracat, Kırklareli, Turkey). This equipment was composed of a laboratory-scale single-screw extruder having a screw diameter of about 25 mm and L/D ratio of 28. It is important to note that the screw design of this equipment was purposely designed to produce significant shear.

The process of manufacturing the filament entailed five distinct steps that included feeding, heating, melting, cooling, and winding of the materials introduced. In the process of feeding, the materials were fed into the hopper of the filament extruder where the melt is heated through the heating zones of the extruder toward the nozzle. Heating zones of the nozzles were set at 180°C, 190°C, 200°C, and 200°C (head zone). Screw speed was kept at 10 rpm. Molten filament coming from the nozzle was cooled by water whose temperature was 45°C ± 3°C, and then it was wound at 40 rpm. Moreover, diameter of the filament was measured using a laser caliper mounted on the extrusion machine whose diameter was 1.74 ± 0.05 mm.

2.2 | Sample Fabrication by 3D Printing

The samples used in this experiment were manufactured through the Raise E2CF 3D Printer (Raise3D Technologies Inc., Irvine, CA, USA). Test samples with the size of 25 × 25 × 4 mm^3 were made from three different types of filament material. Before making the samples, CAD models were prepared first. Then, the samples were sliced using the IdeaMaker software (version 4.3.2, Raise3D Technologies Inc., Irvine, CA, USA). In the manufacturing process, a temperature of 230°C at the nozzle, 60°C at the bed, a printing speed of 40 mm/s, layer thickness of 0.2 mm, and infill density of 100% were used. The raster orientation 45°/−45° was chosen in order to overcome anisotropic phenomena in microstructure development. The samples were printed directly on the platform without any support structure. The automatic bed leveling and bed temperature of 60°C were applied in order to ensure the strong adherence of the first layer. The technical drawing of the wear test specimen with its nominal dimensions and the real photographic view of the as-printed part sample are presented in Figure 1.

2.3 | Thermal Cycling Aging Procedure

Thermal Cycling Aging was performed using an 80-L climatic test chamber (ZUNDAR, model EEXTH 80-U) in the Wear Laboratory of the Faculty of Aviation and Astronautics of Kocaeli University. This climatic test chamber meets the standards of IEC 60068-3-5 and provides a wide temperature range between −70°C and +180°C, with an average heating speed of 4°C/min and cooling speed of 2°C/min. Temperature control is ±2°C, temperature uniformity is ±2°C–3°C, and temperature variation stays under ±1°C. The internal dimensions of the chamber are 400 × 400 × 500 mm and load capability is 30 kg on a stainless-steel shelf.

A thermal cycle was carried out as per IEC 60068-3-5 and was done as follows: specimens were initially heated to 40°C from room temperature having about 50% RH at a rate of 4°C/min, during which time the RH was increased to 98% from 10% in the humidity controllable limit of the chamber, and reached 93% ± 3% RH at 40°C. The specimens were kept at 45 min at 40°C and 93% RH (high-temperature dwell) thus causing combined thermal and hygroscopic stress that enabled diffusion of moisture into the composite matrix and fiber–matrix interfaces. Cooling at the same rate to −20°C then took place and as soon as the temperature reached beyond the controllable humidity range of the chamber, the RH stopped increasing but the condensation and freezing of moisture started on the specimen surface. The specimens were further cooled for 45 min at −20°C (low-temperature dwell). Noncontrollable moisture on the surface resulted in liquid–solid transition (freezing) causing volumetric stresses on the fiber–matrix interface and cracking of PLA matrix. This process can be compared with the frost-wedging phenomenon which influences crack propagation in polymer composites. As soon as the conditions of 40°C and 93% RH with a 4°C/min heating rate were established, the next cycle began. Each cycle took about 120 min with 24 min ramp and 90 min dwells at both high and low temperatures limits. A figure showing the temperature and humidity envelopes for the thermal cycling process is shown in Figure 2.

Two different aging times were used in this research; namely, 200 cycles (equal to 16.7 days) and 400 cycles (equal to 33.3 days). Control specimens were those without aging time (zero cycles). For each specimen-material pair for different aging times, there were three samples taken in order to achieve the reproducibility of results. Thereafter, these samples were loaded into a stainless-steel tray within the furnace.

2.4 | Ball-On-Disk Wear Test

In this experiment, a ball-on-disk setup was used with the UTS Tribolog Multi-Function Tribometer (Istanbul, Türkiye). The

15480569, 0, Downloaded from https://4spepublications.onlinelibrary.wiley.com/doi/10.1002/pc.71528 by Turkey Cochrane Evidence Aid, Wiley Online Library on [14/08/2026]. See the Terms and Conditions (https://onlinelibrary.wiley.com/terms-and-conditions) on Wiley Online Library for rules of use; OA articles are governed by the applicable Creative Commons License

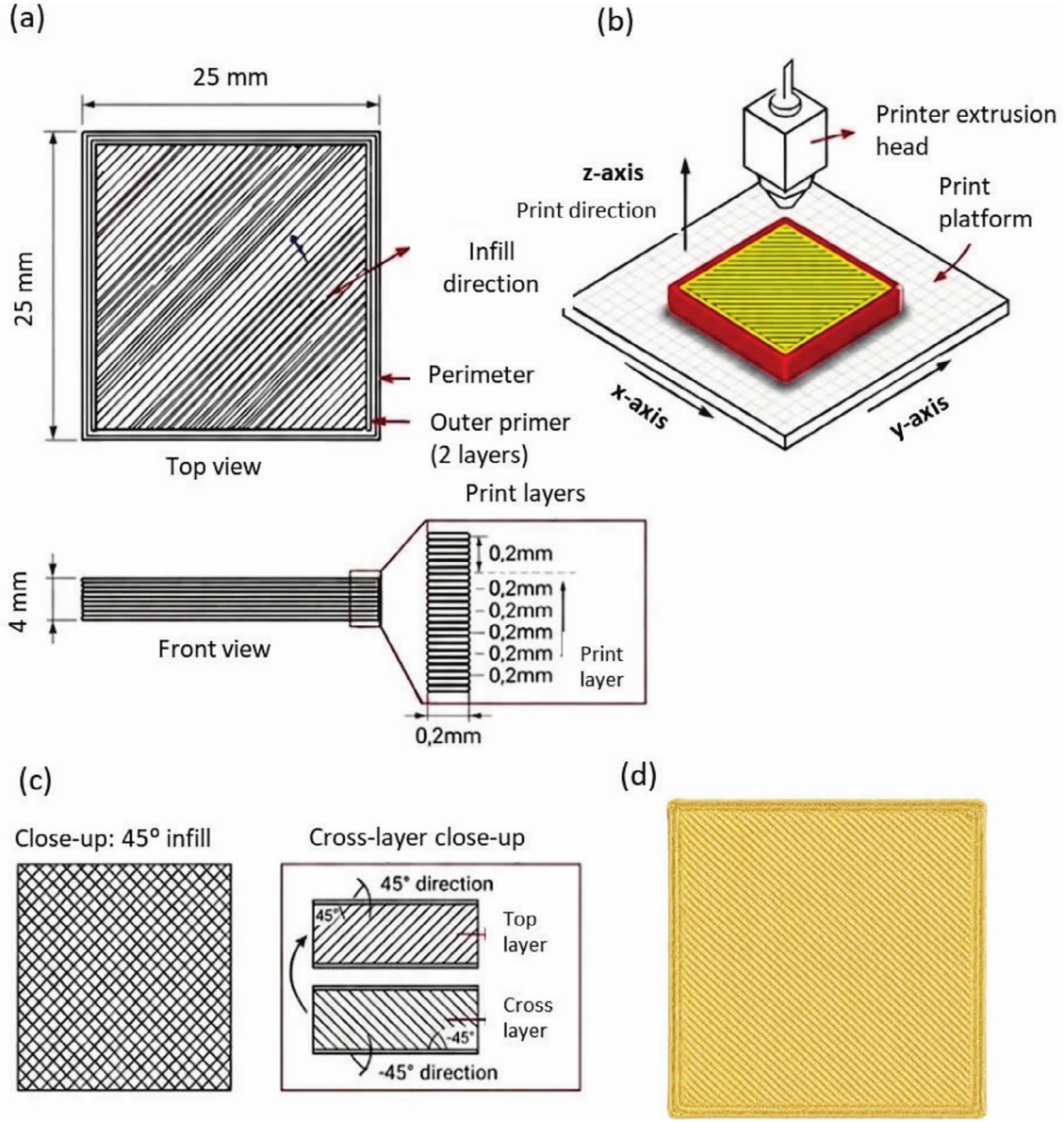

FIGURE 1 | Manufacturing process of the parts: (a) Technical drawing of the wear test specimen ($25 \times 25 \times 4\,mm^3$) with the 45°/−45° raster orientation; (b) print direction and orientation; (c) infill pattern and raster analysis; (d) real view of the as-printed part.

ball-on-disk wear experiments were performed according to the ASTM G99 test procedure, which is a standard test method for wear testing by using a pin-on-disk (ball-on-disk) test rig, in terms of specimen–counterface combination, normal load, sliding velocity, and recording friction and wear results utilized in the present work. In the ball-on-disk test, a stationary counterface, which is a 6 mm diameter 100Cr6 steel ball, was loaded against the flat and circular composite specimen at a fixed normal load of 20 N as the disk rotates, hence resulting in the formation of a circular wear track whose radius depends on the distance from the ball to the rotating axis. The 100Cr6 steel ball (hardness range 60–66 HRC; as-received surface roughness, Ra $< 0.05\,\mu m$) was sliding against the composite specimens. Each specimen and counterface were ultrasonically cleaned in ultrapure isopropanol and air-dried using nitrogen gas before each run. A new ball was installed in each test to avoid contamination and transfer film formed in previous tests.

Each material, pure PLA, PLA with 10 wt% GF, and PLA with 15 wt% GF, was subjected to tests under three thermal cycling regimes (reference condition—0 cycles, thermally aged—200 and 400 cycles) at two linear sliding speeds (50- and 100-$mm\,s^{-1}$). The increased speed was reached through modification of the disk rotation speed at the same track radius. At the same time, the total distance traveled was kept constant at 100 m in order to provide an equal basis of comparison of all the results. Table 1 shows the wear test parameters. Each sample was conditioned for 24 h in the atmosphere with 23°C ± 2°C and 50% ± 5% relative humidity. In addition, new previously unused tracks were used for each experiment to avoid any influence of previous measurements. The COF was measured as a function of sliding distance using the data acquisition system of the tribometer. The wear marks obtained were then analyzed by 3D optical profiling (Section 2.5) to determine the wear scar parameters.

15480569, 0, Downloaded from https://4spepublications.onlinelibrary.wiley.com/doi/10.1002/pc.71528 by Turkey Cochrane Evidence Aid, Wiley Online Library on [14/08/2026]. See the Terms and Conditions (https://onlinelibrary.wiley.com/terms-and-conditions) on Wiley Online Library for rules of use; OA articles are governed by the applicable Creative Commons License

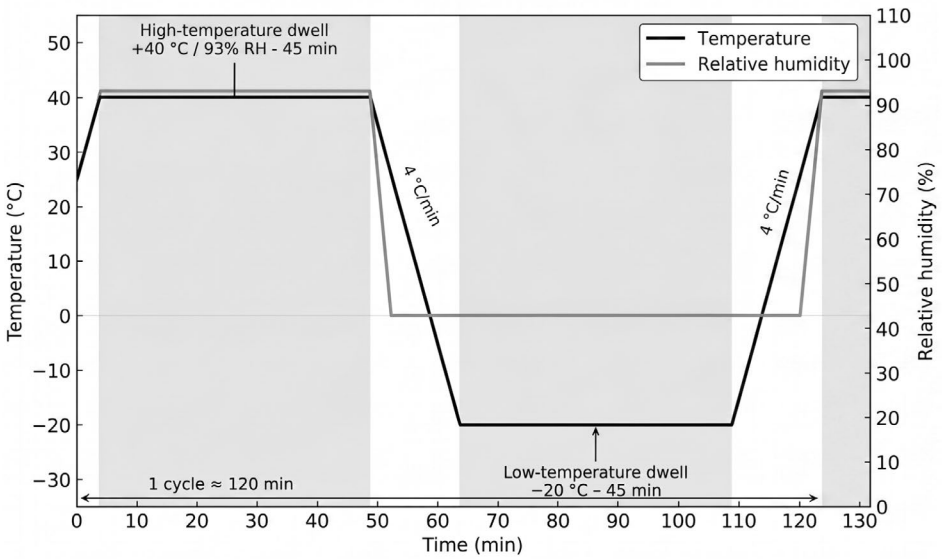

FIGURE 2 | Schematic representation of one complete thermal cycling profile applied in the climatic test chamber.

TABLE 1 | Wear test parameters.

Parameter	Value
Composite type	Pure PLA/PLA + 10 wt% GF/PLA + 15 wt% GF
Normal load	20 N
Sliding speed	50 mm/s, 100 mm/s
Total sliding distance	100 m
Frequency	2 Hz
Thermal cycling aging	Reference (0 cycles)/200 cycles/400 cycles
Counter-body	100Cr6 steel ball (Ø6 mm)

2.5 | Surface Characterization

Surface profiles of the wear marks formed in ball-on-disk tribology after testing were measured using the noncontact laser-based profilometer (Nanovea PS-50, Nanovea Inc., Irvine, CA, USA). It uses the principle of chromatic confocal metrology that avoids any contact between the measurement system and the surface of the sample, preventing further plastic deformation or thermal degradation in the worn region during measurement. All data sets of surface profiles were processed using the Mountains Map software (v. 6.2.7487, Digital Surf), and the areal surface texture parameters (e.g., maximum peak-to-valley height, Sz) were defined and evaluated in accordance with the ISO 25178 series on geometrical product specifications (GPS); surface texture: areal.

The 3D wear-scar topography of each test specimen was created based on the scan data of the surface and used to perform the qualitative evaluation of wear-track morphology. Quantitative wear parameters were calculated based on the representative 2D cross-section of the wear track obtained along the line perpendicular to the sliding direction. Initially, the wear-track periphery was identified in the 2D surface topography projection using the contour-picking feature in Mountains Map software, where the reference plane was specified as the unworn surface plane. Two main wear parameters were determined based on the extracted cross-sectional profile: (a) maximum wear depth (μm), which was the largest distance between the reference plane and the deepest point of the wear scar; and (b) wear-track width (μm), which is the wear groove width at the reference plane level.

For each combination of the type of material, aging treatment, and applied load, five independent measurements were performed at equally spaced positions on the worn area to consider the natural spatial variability in the wear tracks created on the surface of FDM-produced composites. The numeric value presented for each profilometric parameter is the mean value of five measurements conducted under certain experimental conditions. The uncertainty of the profilometric measurement is considered as ±2.9% and is a consequence of the interaction of instrument repeatability, surface heterogeneity in the area of five measurement points, and variation between specimens in each experimental condition. To provide a thorough morphological insight into the process of damage formation as a result of aging treatment, 3D reconstruction of topographical surfaces was obtained for selected experimental conditions.

2.6 | Differential Scanning Calorimeter Analysis

Thermal properties of both pure PLA and GF-reinforced PLA before and after aging were measured via TA Instruments Q200 differential scanning calorimetry (DSC) with nitrogen atmosphere. The values calculated include the glass transition temperature (T_g), cold crystallization temperature (T_c), melting temperature (T_m), enthalpy of cold crystallization (ΔH_c), and enthalpy of melting (ΔH_m). All measurements were performed with a 5°C/min heating rate in a temperature range of 30°C–200°C. The percent relative degree of crystallinity (%) was calculated according to Equation (1) based on the obtained DSC data. In this calculation approach, the net melting enthalpy ($\Delta H_m - \Delta H_c$)

15480569, 0, Downloaded from https://4spepublications.onlinelibrary.wiley.com/doi/10.1002/pc.71528 by Turkey Cochrane Evidence Aid, Wiley Online Library on [14/08/2026]. See the Terms and Conditions (https://onlinelibrary.wiley.com/terms-and-conditions) on Wiley Online Library for rules of use; OA articles are governed by the applicable Creative Commons License

of the unaged pure PLA sample (pure PLA_0 cycles) was used as a standard reference (100%) value and the degree of crystallinity of other samples was normalized according to this standard. Since the content of the polymer varied between composites, the correction for the weight fraction of the GF reinforcement was applied.

$$\left(X_c\right)_{rel=}\left[\frac{\Delta H_m - \Delta H_c}{\Delta H_m^0 \times (1-w)}\right] \times 100 \quad (1)$$

where ΔH_m^0 is the net melting enthalpy of the unaged pure PLA specimen used as the reference value, w is the weight fraction of GF (0, 0.1, and 0.15 for pure PLA, PLA + 10 wt% GF, and PLA + 15 wt% GF, respectively), ΔH_m is the melting enthalpy, and ΔH_c is the cold crystallization enthalpy of each sample.

2.7 | Scanning Electron Microscopy (SEM) Analysis

For the characterization of surface morphology of the tested samples, a desktop scanning electron microscope (SEM), model JCM-6000 (JEOL Ltd., Tokyo, Japan) was used. Before scanning, all samples were subjected to gold coating in order to maintain their surface electrical conductivity. The gold coating was performed at a pressure of 10^{-2} bar using an electric discharge of 30 mA for 120 s.

3 | Results and Discussion

3.1 | COF Examinations

Figure 3 represents the development of the COF (μ) as a function of sliding distance, reflecting a sophisticated dependence between the content of GFs, sliding speed and intensity of thermal aging determining the tribological behavior of FDM-produced PLA composites in all experimentally studied cases. In the unaged state and at 50 mm/s (Figure 3a), the COF profiles demonstrate a well-defined and clear-cut hierarchy with respect to the number of fibers in composite: pure PLA demonstrates the initial run-in transient and subsequent high, relatively unstable steady-state plateau, while composites with 10 and 15 wt% GF successively decrease both the COF level and the fluctuation amplitude. This behavior is related to the increased capability of the GFs to sustain the load and limit the plastic deformation of the matrix, as well as to the reduction of real contact area for adhesive interactions between the matrix and steel surfaces. The increase of the sliding speed up to 100 mm/s (Figure 3b) significantly changes this hierarchy in the unaged condition: the increased generation of frictional heat leads to the increase of interfacial temperature approaching the glass transition point of PLA and causes viscous softening and creation of the thin lubricating transfer layer of matrix material and composite with 10 wt% GF, whereas the compact arrangement of fibers in the 15 wt% GF composite works as abrasive particles against the steel surface, increasing friction and favoring the three-body contacts, hence revealing the optimal content of fibers at this sliding speed.

An analysis of the COF data for unaged samples (Figure 3a,b) demonstrates that the plateaus correspond to the successive contact regimes. For the sliding velocity of 50 mm s^{-1} (Figure 3a), the pure PLA reaches steady state in about 10 m and forms the high plateau with $\mu = 0.45–0.50$; the relatively large plateau height is caused by the continuous formation and breakage of adhesive junctions between the ductile matrix and the steel counterface, as well as the periodical detaching of the material from the track walls. The plateau height of the 10 wt% GF composite is somewhat smaller and smoother because partially exposed fibers start sharing the load in about 15–20 m. The key feature of Figure 3a is the large low-friction plateau of the 15 wt% GF composites, which is maintained at $\mu = 0.10$ for nearly 40 m, prior to the switching to the high steady-state plateau with $\mu = 0.40–0.45$. The delay of the transition can be explained by the dense fiber skeleton on the as-printed surface, which prevents the counterface from entering into the matrix for about 40 m by restricting the contact area to the tip ends of the fibers and blocking the adhesion between the matrix and the steel. At the sliding velocity of 100 mm s^{-1} (Figure 3b), the shape of the plateaus is quite the opposite. The pure PLA provides an unusually low and smooth plateau at $\mu = 0.05–0.08$ for about 75–80 m, after which the COF increases sharply up to $\mu = 0.35–0.40$; the reason for such behavior is the rapid heating of the contact due to the higher sliding velocity, which drives the near-surface temperature to the glass transition region of PLA and creates a thin, viscously softened polymer transfer film providing low-friction solid lubrication, until the growing depth of the track and the debris accumulation lead to the termination of the low-friction regime. The 10 wt% GF composite provides a shorter low-friction plateau with the gradual transition from $\mu = 0.15–0.20$ to $\mu = 0.40–0.45$ starting approximately at 40–60 m, due to the localized disruption of the continuity of the film by the fibers embedded in the matrix. In contrast, the 15 wt% GF composite loses its low-friction phase almost instantly (in about 10–30 m) and moves to the highest and most fluctuating plateau of the unaged series with $\mu = 0.40–0.45$; this happens due to the dense, hard fiber skeleton on the as-printed surface, which prevents the formation of the cohesive film, leading to the micro-abrasive contact of multiple asperities against the steel ball. Thus, the data presented in Figure 3a,b show that the fiber skeleton, which delays matrix engagement and lowers the friction at 50 mm s^{-1}, acts as a disruptive film-forming barrier at 100 mm s^{-1}; it is this mechanism that underlies the speed-dependent reversal of the COF hierarchy. It is important to mention that all these interpretations of transfer film formation were done based on the characteristics of the COF curves as well as on the SEM pictures of the sample side; however, a characterization of the counterpart surface was not done because in each test a new ball was used.

The 200 thermal cycles at 50 mm/s (Figure 3c) induce moisture absorption, residual thermal stresses and the initiation of microcracks in pure PLA matrix, shown as the increase of the COF amplitude revealing the process of delamination, while the GF composites demonstrate relatively stable COF traces due to the ability of fiber skeleton to resist cracks. Interestingly, the 15 wt% GF composite demonstrates the most stable COF profile in the entire low-speed dataset under these conditions, being a consequence of the moderate plasticization of PLA material at the contact point with minimal damage. At 100 mm/s and after 200 thermal cycles (Figure 3d), pure PLA shows highly unstable COF profile with high value of friction, revealing the increased brittleness of material and degradation of the interface, while the

15480569, 0, Downloaded from https://4spepublications.onlinelibrary.wiley.com/doi/10.1002/pc.71528 by Turkey Cochrane Evidence Aid, Wiley Online Library on [14/08/2026]. See the Terms and Conditions (https://onlinelibrary.wiley.com/terms-and-conditions) on Wiley Online Library for rules of use; OA articles are governed by the applicable Creative Commons License

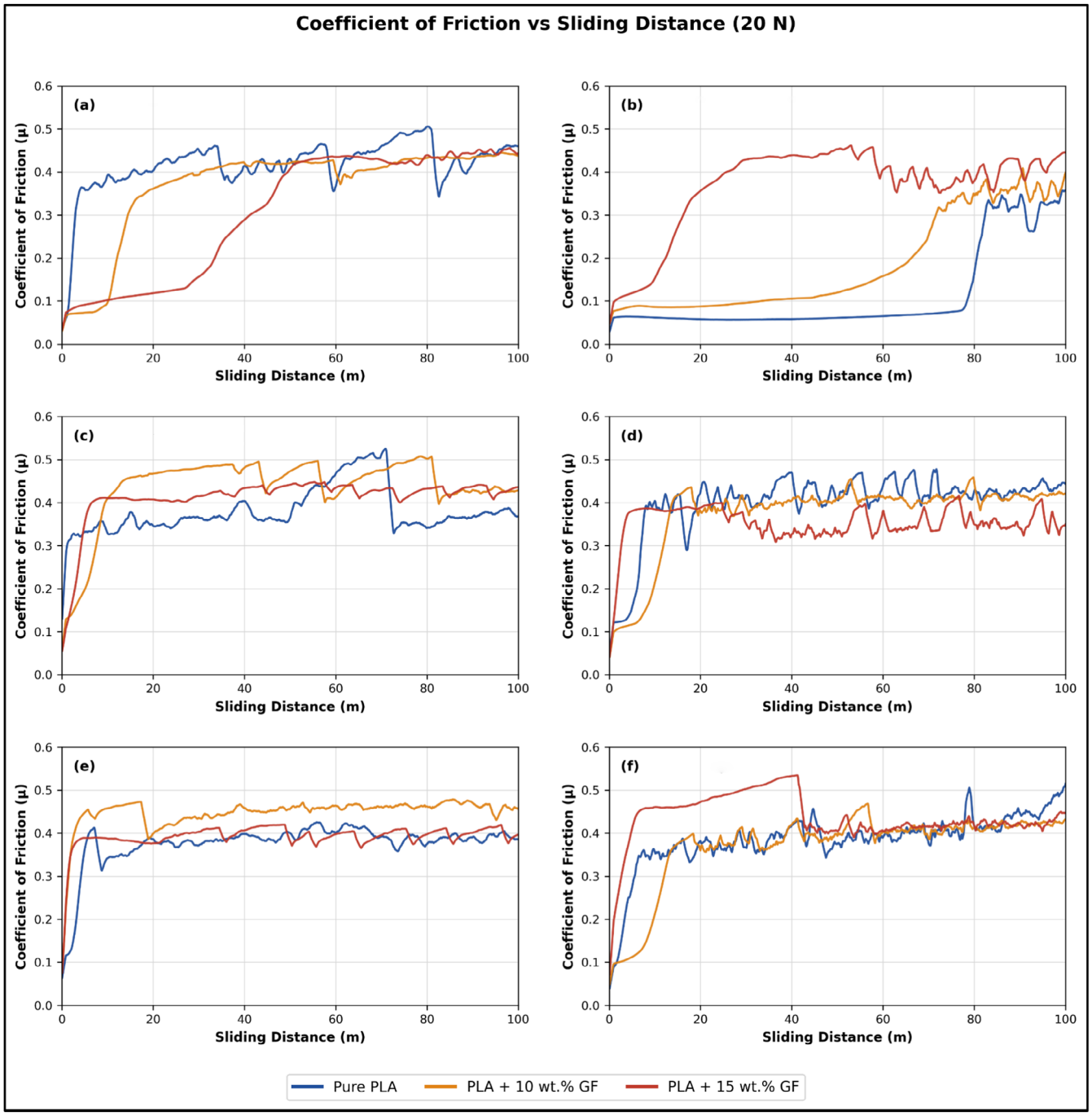

FIGURE 3 | Evolution of the coefficient of friction (μ) as a function of sliding distance: (a) Friction behavior at a sliding speed of 50 mm/s for the reference (0 cycles) specimens; (b) friction behavior at a sliding speed of 100 mm/s for the reference (0 cycles) specimens; (c) friction behavior at a sliding speed of 50 mm/s after 200 thermal cycles; (d) friction behavior at a sliding speed of 100 mm/s after 200 thermal cycles; (e) friction behavior at a sliding speed of 50 mm/s after 400 thermal cycles; (f) friction behavior at a sliding speed of 100 mm/s after 400 thermal cycles.

two composites possess lower mean COF values and higher fluctuations corresponding to the multi-asperity contact mechanism when the load is transferred through a wider contact area. This transformation explains the fact that the 10 wt% GF composite has higher COF stability at this speed than the 15 wt% GF one, similarly to Figure 3b. Figure 3e presents the largest discrepancy in tribological response within the entire dataset: after 400 thermal cycles at 50 mm/s, the COF profile of pure PLA becomes severely unstable with the high-amplitude spikes attributed to the third body abrasion of fracture fragments, while the 15 wt% GF composite retains low and stable COF trace, demonstrating the effect of the GF reinforcement on the improvement of wear resistance and thermal cycling performance in the low-speed regime even in the most aged state. Figure 3f contains the most significant mechanistic result of the work: after 400 thermal cycles at 100 mm/s, the COF profiles of all three materials have almost equal mean values with high variability, revealing the regime change caused by the maximum frictional heating, embrittlement of the matrix and deterioration of interfaces and leading to the loss of the reinforcing effect of GF addition.

15480569, 0, Downloaded from https://4spepublications.onlinelibrary.wiley.com/doi/10.1002/pc.71528 by Turkey Cochrane Evidence Aid, Wiley Online Library on [14/08/2026]. See the Terms and Conditions (https://onlinelibrary.wiley.com/terms-and-conditions) on Wiley Online Library for rules of use; OA articles are governed by the applicable Creative Commons License

The destruction of the hierarchy identifies the crosspoint of the high sliding speed and the maximum thermal aging as the critical operational state in FDM-produced PLA composites.

The tribological behaviors seen in Figure 3 conform to and can be explained by current literature concerning fiber-reinforced polymer composites exposed to different sliding conditions and environmental aging. Speed-dependent change in the hierarchy of the COF values, where higher GF percentage is advantageous at 50 mm/s but disadvantageous at 100 mm/s is almost identical to that described by Liow et al. [29], where an increase in the linear speed of sliding of FDM-printed PLA/GF composites against steel systematically lowers the COF. It occurs as a result of accumulation of the frictional heat at the sliding interface, causing softening of the surface layer of the PLA matrix and formation of a thin transfer layer. Most importantly, it was found by the authors that reinforcement with GF leads to an increase in COF compared to PLA alone at the same speed owing to mechanical locking of the asperities of the latter and three-body contact; this process becomes even more pronounced with increase in GF content, thus explaining the COF inversion seen in Figure 3b,f of the current paper. Frictional heat being the main driver of the COF of FDM-printed PLA against steel is additionally confirmed by the findings of Palaniandy et al. [30] who found that for sliding speeds in the range of 0.46 to 0.81 m/s, the COF of 3D-printed PLA monotonically decreases with increasing speed due to temperature rises at the point of contact causing softening of the polymer and material flow. Such a thermal softening mechanism stands behind the transfer-layer formation that causes the decrease of the COF of the pure PLA and 10% GF composite at 100 mm/s in Figure 3b, whereas at high speeds the softening of the material results in melting of it, breaking the trend and causing high-amplitude COF oscillations typical for melt-contact state, similarly to those seen in the present paper for maximum aging and sliding speeds (Figure 3f). Increasing instability of COF traces during thermal aging of the materials seen as the growth in their amplitude in pure PLA and, in case of high speed and aging, in the composites, matches well with the results obtained by Autay et al. [31] studying the effects of hygrothermal aging on short GF-reinforced Poliamid 66 (PA66) and found that the accelerated aging systematically leads to reduction in flexural matrix strength and increased COF. According to the authors, such a change is caused by plasticization of the polymer by moisture at the fiber–matrix interface, interfacial debonding and debris production changing the mechanism of wear from ductile smoothening to abrasive three-body contact, exactly the same degradation processes that have been traced from the COF traces in Figure 3a–f in the present study. Finally, the finding that thermal aging can invert the tribological hierarchy of the material grades where the 10% GF composite demonstrates the deepest wear and the least stable COF among all three materials after 400 cycles at 100 mm/s has its confirmation in the work of Sahin et al. [32]. In the paper the authors show that the short-term thermal aging cycles of GF-reinforced polyamide composites lead to considerable changes in wear properties, while causing only small changes in the COF. The reason given by the authors is that the thermal embrittlement causes the thinning of the load-carrying polymer layer leading to the earlier contact of abrasive GFs with steel substrate. It results in both increased friction coefficient and wear of the surface layer.

3.2 | Profilometric Analysis of Wear-Track Damage

Figure 4 shows the topographical 3D profilometry images of representative wear scars produced under a fixed loading of 20 N and sliding speed of 50 mm/s ($X = Y = 8000\,\mu m$). The arrangement of images is designed such as to single out the combined influence of GF reinforcement and thermal cycling aging on wear properties. Figure 4a illustrates that unaged pure PLA has a well-formed, smooth, bowl-shaped wear track, composed of concentric plowing bands and characterized by the maximum depth of 198 μm, track width of 853 μm, and maximum peak-to-valley height (Sz) of 287.6 μm. The regular groove and lack of detached debris indicate wear behavior controlled by plastic deformation and abrasive plowing with a partial involvement of localized adhesive/thermal smearing as characteristic for an unreinforced polymer matrix. Figure 4b demonstrates the most disturbed and worst-looking topography among the four cases, where 400 thermal cycles result in the increased maximum depth of pure PLA up to 217 μm, track width—to 910 μm, and Sz nearly doubled to 567.1 μm. The crater looks irregular and has pronounced pile-ups and detached debris, indicating a shift from ductile plowing toward brittle fracture and delamination. This is obviously the worst case, corresponding to thermally induced embrittlement and loss of load-bearing properties in the unreinforced matrix. Figure 4c illustrates the lowest damage among the four cases, where the unaged 15 wt% GF composite has shallow and narrow wear track (maximum depth 65 μm, width 510 μm), where the initial raster pattern is clearly observed. Despite the texturized and fiber-rich surface increases Sz to 490.3 μm, the very low wear scar area (wear-scar area 0.06 mm^2, which is about one-fifth of that of pure PLA) confirms the role of GFs as load-bearing skeleton preventing indentation and abrasive penetration. This is the best wear behavior demonstrated. Figure 4d shows that, even under maximal aging, the 15 wt% GF composite retains shallow and well-confined wear track (maximum depth 81 μm, width 533 μm, Sz = 321.2 μm), where the raster pattern is still preserved. Only slightly larger values compared to the unaged composite demonstrate the stability of dimension and thermal properties of the reinforced composite under thermal cycling, in contrast to pure matrix. In general, the interpretation of the matrix by rows shows the influence of thermal cycling, whereas by columns shows the influence of fiber reinforcement. Thermal cycling strongly affects wear behavior of pure PLA (Sz: 287.6; 567.1 μm; wear-scar area: 0.29; 0.36 mm^2), but insignificantly influences the 15 wt% GF composites (0.06; 0.09 mm^2). In general, GF reinforcement decreases wear depth and removed material area about 3–5 times and suppresses the aging-induced wear that occurs in the unreinforced matrix. Thus, the transformation from deep and debris-rich crater of aged pure PLA (Figure 4b) to shallow and raster-patterned wear track of aged composite (Figure 4d) proves visually the enhancement of both wear and thermal cycling properties of GF reinforcement.

Figure 5 demonstrates the three-dimensional profilometric topographies of the wear scars generated during sliding at the increased sliding speed of 100 $mm\,s^{-1}$ with the constant applied load of 20 N ($X = Y = 8000\,\mu m$) between the pure PLA and the PLA + 10 wt% GF composite in two opposite states without (0 cycles) and after (400 cycles) the aging procedure. Figure 5a proves

15480569, 0, Downloaded from https://4spepublications.onlinelibrary.wiley.com/doi/10.1002/pc.71528 by Turkey Cochrane Evidence Aid, Wiley Online Library on [14/08/2026]. See the Terms and Conditions (https://onlinelibrary.wiley.com/terms-and-conditions) on Wiley Online Library for rules of use; OA articles are governed by the applicable Creative Commons License

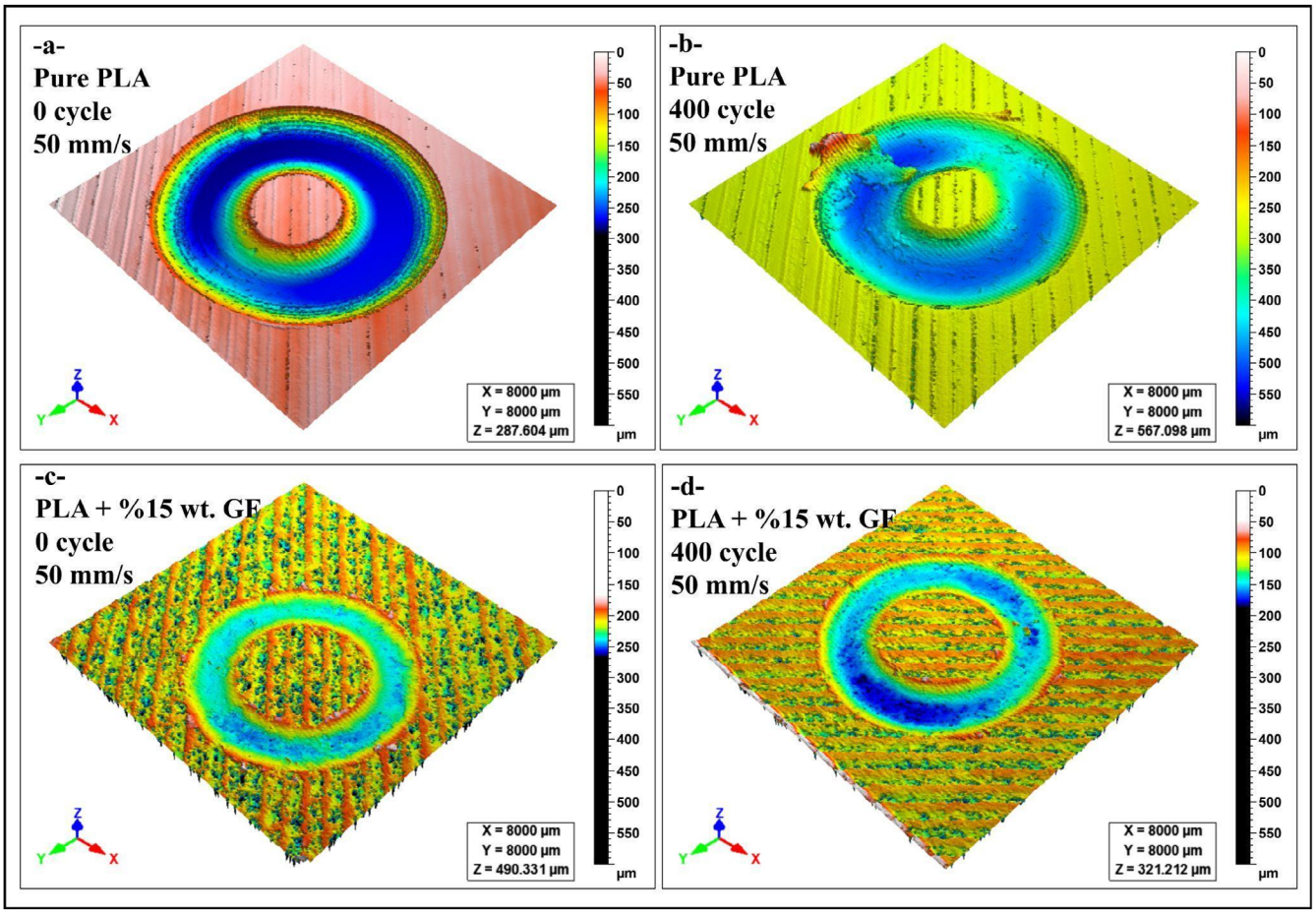

FIGURE 4 | Comparison of profilometric 3D surface images of ball-on-disk wear scars at 20 N load, 100 m track with 50 mm/s sliding speed: (a) pure PLA, 0 cycle; (b) pure PLA, 400 cycle; (c) PLA + 15 wt% GF, 0 cycle; (d) PLA + 15 wt% GF, 400 cycle.

that the unaged pure PLA demonstrates rather shallow ring-shaped wear track with a maximum depth of 103 µm, a width of 650 µm, and a maximum peak-to-valley height (Sz) of 480.7 µm, which means that it undergoes moderate and uniformly distributed wear mainly associated with light abrasive plowing. Figure 5b demonstrates that the aging causes deepening (to 174 µm) and widening (to 1000 µm) of the pure-PLA wear track, which leads to an increase of Sz up to 658.2 µm and a surface area of the wear scar of 0.24 mm^2; the wear scar becomes much wider and deeper, which means that aging leads to embrittlement and loss of load-carrying properties of the matrix, though the wear is still relatively even. Figure 5c presents the least pronounced topography among the considered samples, since the unaged 10 wt% GF composite forms the shallow and narrow wear scar (maximum depth 96 µm, width 740 µm, Sz = 424.9 µm) with the printed raster pattern still being visible, which confirms that the GFs prevent the penetration effectively and provide the best wear resistance at this speed. Figure 5d presents the most damaged and disrupted topography of all samples tested within the study: after 400 thermal cycles, the same 10 wt% GF composite forms the deepest crater (209 µm), the highest Sz (716.5 µm), and the largest area of the removed material (0.31 mm^2); the crater is bordered by the prominent central island of pile-ups and detached fragments, which evidences severe and brittle wear assisted by the third body. Thus, the analysis by columns presents the impact of fiber reinforcement, while the analysis by rows presents the impact of aging procedure. As seen in the unaged state (Figure 5a,c), the 10 wt% GF composite demonstrates slightly lower wear compared to pure PLA (Figure 5a). After aging procedure (Figure 5b,d), the order changes, and the aged 10 wt% GF composite (Figure 5d; 209 µm, Sz 716.5 µm) demonstrates much larger wear (in terms of wear depth and Sz) compared to the aged pure PLA (Figure 5b; 174 µm, Sz 658.2 µm). It can be concluded that at the increased speed of 100 mm s^{-1}, the reinforcing fibers no longer demonstrate their beneficial effect in case of aging.

Figure 6 illustrates the comparison between cross-sections of wear grooves for the three materials (pure PLA, PLA with 10 wt% GF, and PLA with 15 wt% GF) subjected to the same applied load of 20 N. Graphs utilize common depth and lateral scales to illustrate the results of sliding speed (50 mm s^{-1} in the left column and 100 mm s^{-1} in the right column) and thermal cycling aging (0, 200, and 400 cycles, from top to bottom) influence on groove geometry. Figure 6a shows that for the unaged state and 50 mm s^{-1} sliding speed, both groove depth and width decrease consistently with increasing fiber content: pure PLA (198 µm depth, 853 µm width) > 10 wt% composite (117 µm) > 15 wt% composite (65 µm depth, 510 µm width). This leads to the clear hierarchical relation between the materials when increasing the amount of reinforcement results in narrowing and shallowing of wear scar. Figure 6b reveals that for 100 mm s^{-1}

15480569, 0, Downloaded from https://4spepublications.onlinelibrary.wiley.com/doi/10.1002/pc.71528 by Turkey Cochrane Evidence Aid, Wiley Online Library on [14/08/2026]. See the Terms and Conditions (https://onlinelibrary.wiley.com/terms-and-conditions) on Wiley Online Library for rules of use; OA articles are governed by the applicable Creative Commons License

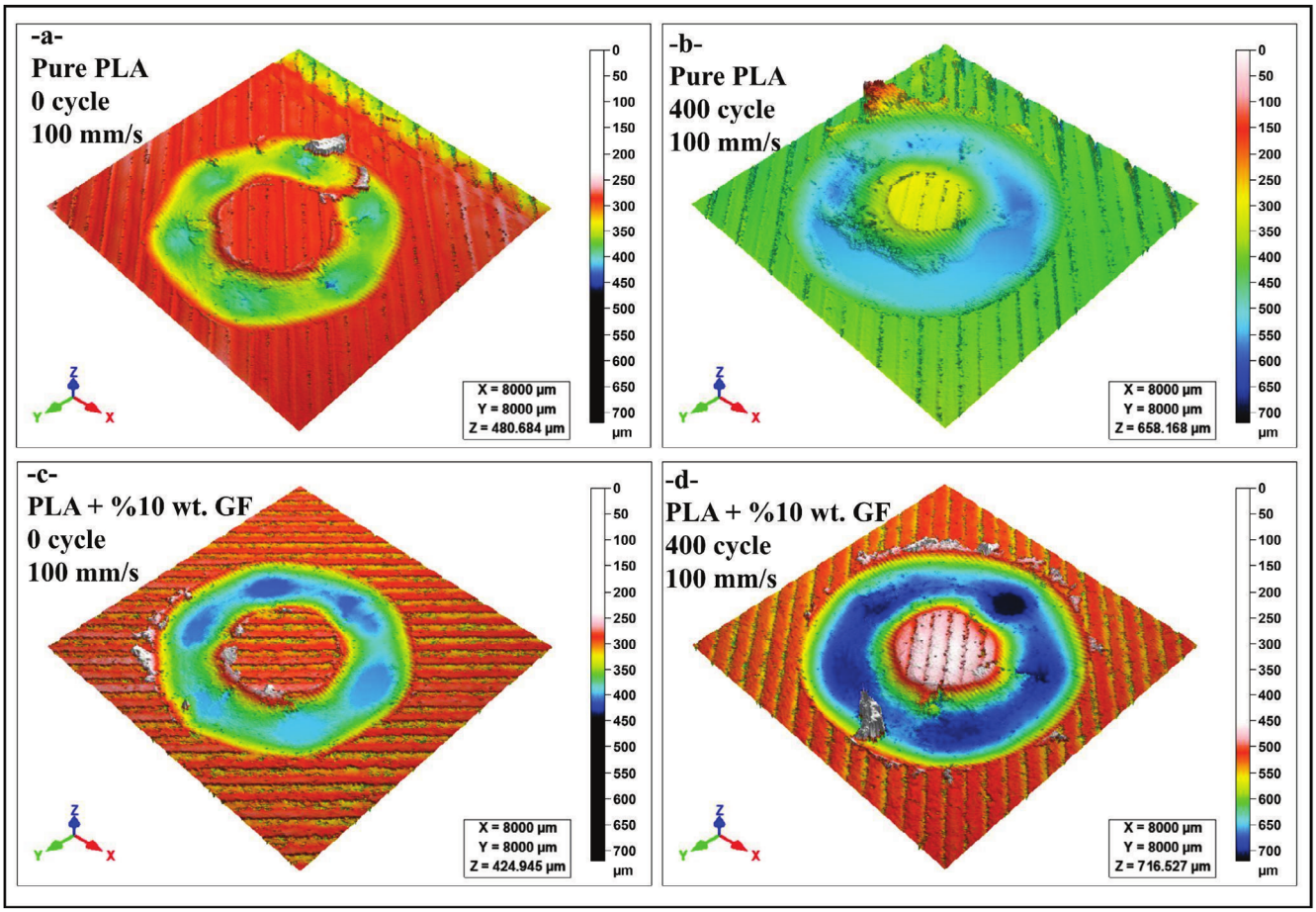

FIGURE 5 | Comparison of profilometric 3D surface images of ball-on-disk wear scars at 20 N load, 100 m track with 100 mm/s sliding speed: (a) pure PLA, 0 cycle; (b) pure PLA, 400 cycle; (c) PLA + 15 wt% GF, 0 cycle; (d) PLA + 15 wt% GF, 400 cycle.

sliding speed in the unaged state, this hierarchical relationship is broken, where pure PLA and 10 wt% composite possess comparably shallow grooves (103 and 96 µm, correspondingly), while 15 wt% composite makes the deepest groove (150 µm). This inversion demonstrates that without aging, increased frictional heating and fiber–counterface interaction overcome the protective effect of the highest fiber concentration. Figure 6c proves that the protective hierarchy demonstrated in Figure 6a becomes stable and strengthened after 200 thermal cycles at 50 mm s^{-1}, when the depths of grooves for pure PLA, 10 wt% composite and 15 wt% composite are equal to 217, 115, and 52 µm correspondingly, the last being the shallowest profile in the group—it demonstrates the stability of the fiber-enriched surface in an intermediate aged condition. Figure 6d shows that at 100 mm s^{-1} sliding speed and after 200 thermal cycles, pure PLA possesses the deepest groove (189 µm), while the two composites demonstrate shallower depths of grooves (102–112 µm) with broader tracks (up to 1130 µm for 10 wt% composite), which points to the transition to wider and shallower wear profile for reinforced materials. Figure 6e demonstrates that the consistent fiber-dependent ranking remains for the most aged condition of 400 cycles at 50 mm s^{-1} with depths decreasing from pure PLA (217 µm) to 10 wt% composite (177 µm) to 15 wt% composite (81 µm), thus proving that even after maximum thermal cycling the highest fiber loading gives rise to the shallower and narrower wear track. Figure 6f shows that at 100 mm s^{-1} sliding speed and after 400 thermal cycles, there is a convergence of the three profiles, when depths become comparable (pure PLA 174 µm, 10 wt% composite 209 µm, 15 wt% composite 182 µm), which suggests that the combination of high speed and advanced aging almost eliminates material dependence. In general, the left column shows that for 50 mm s^{-1} sliding speed the fiber reinforcement consistently acts as protection in all aged states, where 15 wt% composite provides the shallowest and narrowest groove in all cases. In turn, the right column demonstrates that for 100 mm s^{-1} sliding speed the protective effect becomes less and less pronounced, until convergence of curves is reached after 400 cycles. Thermal cycling generally increases depths and widths of tracks in all materials, with pure PLA exhibiting the biggest changes at low speed.

Profilometric observations of the systematic changes in depth, width, Sz value, and removed material area in function of GF content, sliding speed, and aging severity presented in Figures 4–6 are consistent and significantly extend relevant findings in the contemporary literature on tribology of fiber-reinforced polymers. Monotonic decrease in wear depth and scar area for increasing GF content measured at 50 mm/s under all aging severities (Figure 6, left column), where 15 wt% GF composites always display the shallowest and narrowest groove, is fully consistent with the load-bearing skeleton model by Birleanu et al. [33]. Their 3D optical profilometry of GFRP disk wear against 52,100 steels showed that the increase in fiber weight fractions leads to the decrease in track depth and

15480569, 0, Downloaded from https://4spepublications.onlinelibrary.wiley.com/doi/10.1002/pc.71528 by Turkey Cochrane Evidence Aid, Wiley Online Library on [14/08/2026]. See the Terms and Conditions (https://onlinelibrary.wiley.com/terms-and-conditions) on Wiley Online Library for rules of use; OA articles are governed by the applicable Creative Commons License

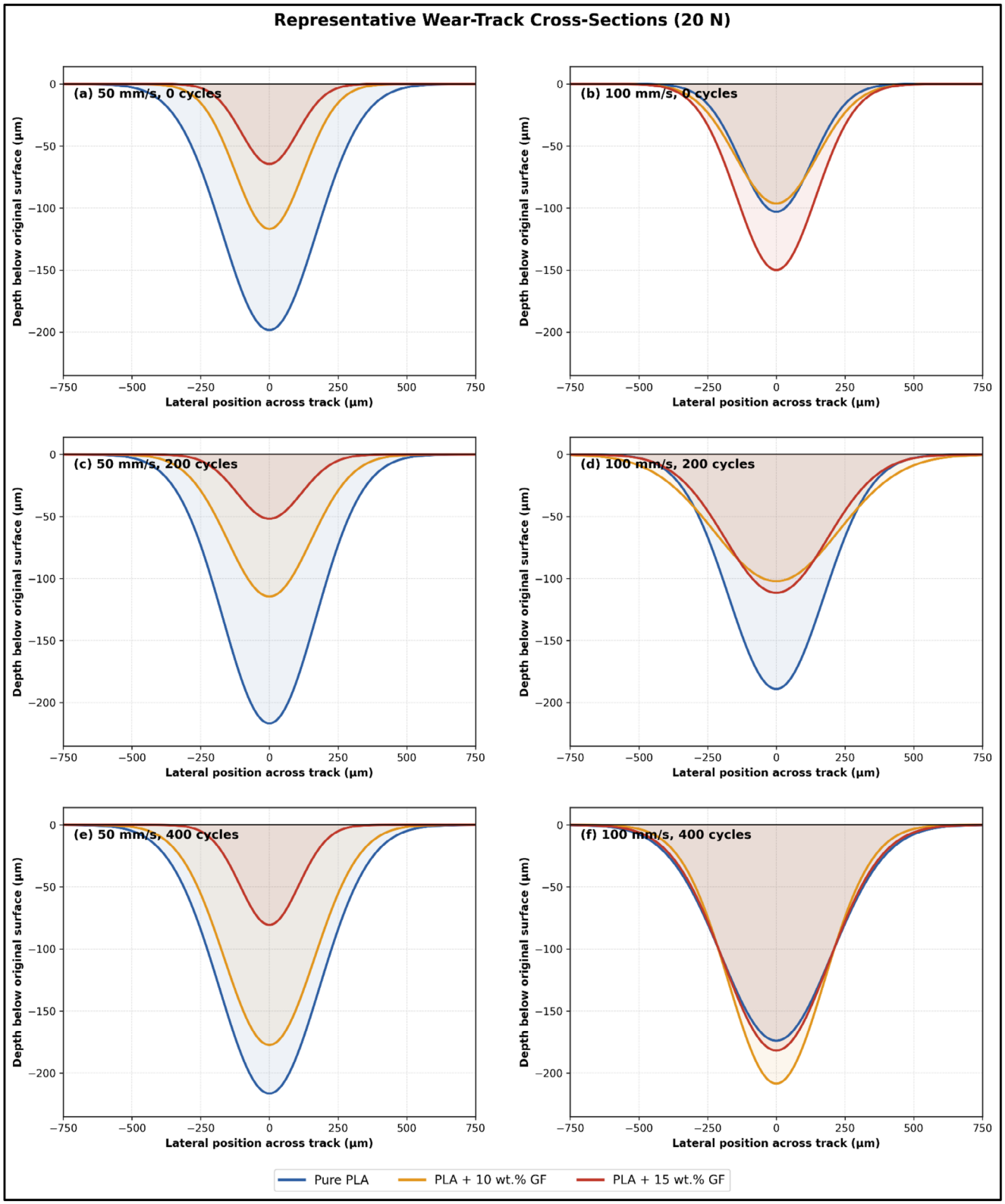

FIGURE 6 | Comparison of profilometric cross-sectional images of ball-on-disk wear scars at 20 N load, 100 m track with: (a) at a sliding speed of 50 mm/s for the reference (0 cycles) specimens; (b) at a sliding speed of 100 mm/s for the reference (0 cycles) specimens; (c) at a sliding speed of 50 mm/s after 200 thermal cycles; (d) at a sliding speed of 100 mm/s after 200 thermal cycles; (e) at a sliding speed of 50 mm/s after 400 thermal cycles; (f) at a sliding speed of 100 mm/s after 400 thermal cycles.

removed material area owing to the predominance of protruding fiber tips responsible for carrying the majority of the applied normal load and hence reducing the indentation depth of the opposing surface in soft polymer matrix. They also mentioned the evolution in wear of profilometric cross-sections from deep and smooth plowing track to wider and shallower scar for an

15480569, 0, Downloaded from https://4spepublications.onlinelibrary.wiley.com/doi/10.1002/pc.71528 by Turkey Cochrane Evidence Aid, Wiley Online Library on [14/08/2026]. See the Terms and Conditions (https://onlinelibrary.wiley.com/terms-and-conditions) on Wiley Online Library for rules of use; OA articles are governed by the applicable Creative Commons License

increase in fiber density, which is perfectly represented in Figure 6a,c of the current study. The degradation in geometry of wear scars for the pure PLA specimens with increasing thermal aging manifested primarily in the doubling of Sz from unaged 287.6 μm to 400 cycle 567.1 μm shown in Figure 4 and expansion of debris-bound crater-like shape of wear scar, can be considered as consistent with the aging effect of Fidan et al. [34] on wear scars of GF polyester laminates by means of ball-on-disk test. Their 3D profilometric characterization of surface metrology revealed that environmental aging causes the systematic increase in wear scar width and depth from 1.38 to 1.90 mm and from 75 to 117 μm, correspondingly, due to matrix embrittlement and fiber–matrix interphase degradation. As a result of such a process, the dominant wear mechanism changes from minor abrasive plowing to severe fracture, causing virtually complete disappearance of low-friction run-in phase, which is consistent with the irregular and debris-piled borders of scars of most aged PLA specimens in Figure 4b. Wear profile transformation during the change of COF state in FDM-printed PLA from smooth run-in plateau to irregular profile with high variability due to transition from ductile plowing to brittle fracture is similar to the stages of tribological behavior of multicomponent FDM-printed PLA system studied by Yilmaz et al. [35]. They characterized the three-stage evolution (run-in, steady-state, and accelerated wear) by the COF versus distance graph cross-referenced by wear volumes and SEM analysis and concluded that the transition between stages occurs due to the structural state of the near-surface contact layer. Their conclusion about maintenance of lower and more constant COF plateau for filler-reinforced FDM-PLA specimens in comparison with pure PLA directly supports the interpretation of the profilometric data in Figure 6a through Figure 5e, where the 15 wt% GF composite always shows the shallowest and narrowest scar under all low-speed conditions. More importantly, the inversion of ranking in Figures 6f and 5d, where the 10 wt% GF composite shows the deepest groove (209 μm) and highest Sz (716.5 μm) of the whole experiment for maximum aging at 100 mm/s, exceedingly even aged pure PLA, finds its direct analogy in the pressurized water aging experiment by Fidan et al. [36] on FDM-printed PLA/GF composites. Their 3D profilometric analysis showed that for maximum aging time the protective benefit of GF is completely exhausted and the wear depth of both 10 and 15 wt% GF composites converges toward, or exceeds, that of pure PLA, with the immersion time being responsible for 76% of the total variation in scar width. Such observation establishes the environmental degradation of the fiber–matrix interface either due to moisture absorption or aging cycles as the common mechanistic origin of protective hierarchy inversion observed profilometrically in the current study for the most extreme loading conditions.

Such observations can be extended to other filament combinations, besides GF/PLA and GF/polyester ones, which are made of thermoplastic filament and subjected to material extrusion during printing. For instance, according to the results of studies conducted by Ergene and Bolat [37], the COF of PETG pins in pin-on-disk tests varied from 0.23 to 0.35, which proves that friction was not associated with the infill rate or build orientation but correlated with the layer thickness increase caused by the rise in surface roughness and number of contact points. This decoupling of friction from the process variables is similar to the COF trends seen in unaged PLA/GF composites (Figure 4a,c,e): in this case, the hierarchy of COFs was defined primarily by the fiber skeleton but not sliding velocity alone and turned disorderly only after thermal aging degraded the surface/interfacial properties of the composites. In another study, Phogat et al. [38], who used GA-ANN optimization of FFF-printed PLA, ABS and PLA/ABS multi-material specimens, reported that PLA had always had the lowest specific wear rate among these three filaments and that the extrusion temperature and infill density, which define the interlayers' integrity and porosity, were the major contributing factors to wear while not the raster angle or printing speed. Such a result is consistent with the natural wear-resistance of the unaged pure-PLA matrix observed in this study and supports interpreting the wear hierarchy changes of the current study based on reinforcement and thermal aging as dependent on the interlayers'/interfacial integrity rather than kinematic test parameters alone. Bolat and Yıldırım [39], who studied wear coupons of PA6, PA6-CF, ABS and ABS-CF, have reported the COF values of 0.42–0.61, which are considerably higher than the 0.23–0.35 range seen for PETG and similar to the higher COF values of the pure PLA in the current study under the high sliding speed and severe thermal aging. Most importantly, they have shown that carbon-fiber reinforcement increased wear resistance of specimens in dry conditions but lost or even reversed this advantage when the specimens were subjected to the NaCl solution conditioning and testing at the highest applied load, where reinforced samples became more prone to the mass loss than the unreinforced matrix. Such inversion of the hierarchy of reinforcement under the combined influence of environmental conditioning and increased severity of testing is directly analogous to the one observed in this study, where 10 wt% and, at the most severe conditions, effectively 15 wt% GF composites lost the advantage over pure PLA in the presence of thermal cycling and high sliding speed (Figure 6d,f). Lastly, Lemecha et al. [40], who investigated FDM-printed PA-12 via ball-cratering, reported that the increase in the extrusion temperature decreased wear under abrasive-slurry contact due to the enhanced interlayer cohesion and lower porosity but resulted in the opposite tendency under dry friction due to the same porosity decrease leading to an increase in the effective contact area in adhesive wear. Such a mechanistic inversion; which is driven by the shift in the dominant wear mechanism between the two regimes; has many parallels to the results of the current study, where a single parameter, either sliding speed or thermal-aging level, inverts the hierarchy of wear resistance of the materials being tested depending on whether fiber-supported plowing or third body abrasion by the fiber pull-out and matrix debris is dominant. Overall, all four studies, including the ones with PETG, PLA/ABS multi-material, PA6/ABS-CF and PA-12 filaments, prove that (a) COF is more strongly controlled by interlayer/interfacial quality than process or kinematic parameters, and (b) advantages in reinforcement-based wear resistance seen under benign conditions are not automatically transferable to the severe thermal, environmental and high-speed sliding regimes.

3.3 | Microstructural Examination of Wear Damages

To complement the profilometric findings and determine the wear mechanism at the fiber and matrix level, SEM images of

15480569, 0, Downloaded from https://4spepublications.onlinelibrary.wiley.com/doi/10.1002/pc.71528 by Turkey Cochrane Evidence Aid, Wiley Online Library on [14/08/2026]. See the Terms and Conditions (https://onlinelibrary.wiley.com/terms-and-conditions) on Wiley Online Library for rules of use; OA articles are governed by the applicable Creative Commons License

the ball-on-disk wear track under low magnification (×24) at unaged (0 cycles) and most heavily aged (400 cycles) states for the three grades of materials have been captured and presented in Figure 7. The testing was performed at a sliding velocity of 100 mm/s.

The unaged pure PLA wear scar is shown in Figure 7a, where the sliding contact leaves behind a well-formed and continuous groove pattern of parallel and evenly spaced plowing lines of identical depth stretching across the whole length of the wear scar. This is bounded by a smooth and continuous rim composed of displaced matrix material and no visible cracks or particulates are found in this area. This morphological structure, consisting of regularly spaced longitudinal grooves due to repeated passage of asperities of the counterface through the contact, is typical of wear mechanisms controlled by plastic-deformation-induced abrasive plowing. The above is corroborated by the moderately deep profile of the wear scar and its smooth, bowl-shaped cross-section determined profilometrically. In Figure 7b, the unaged PLA + 10 wt% GF composite is presented. In comparison with pure PLA, the wear scar is smaller in width and the plowing grooves are unevenly spaced and irregular in their width and depth, showing a torn and rough groove floor and fragmented rim, contrary to the smooth pile-up of the unmodified matrix. Such a transition of wear from smooth and uniform plowing to irregular groove pattern is due to the interference of matrix sliding by embedded GFs, which cause the matrix to locally reinforce the contact and force the counterface to plow through and around the embedded fibers. The mild bridging of fibers and the reinforcing effect result in smaller scar width in comparison with pure PLA. In Figure 7c, the unaged PLA + 15 wt% GF composite is presented. It can be observed that the wear scar is the smallest one among the unaged samples and the surface texture differs significantly from the previous ones in that there are no continuous plowing grooves anymore; instead, the surface consists of a dense granular network formed by GFs and only very short and discontinuous furrows are present. This is consistent with the dense packing of GFs, forming a rigid load-bearing skeleton and restricting the penetration of the counterface into the matrix. The fragmented texture of the surface, together with small dimensions of the wear scar, indicate that the highest fiber concentration results in the greatest resistance to material removal in the unaged series. Figure 7d illustrates the pure PLA specimen subjected to 400 thermal cycles. Here the wear scar is bounded by an extensive crack network and flakes of matrix material radiating outward from the groove. This is unlike the smooth and intact periphery of the unaged sample shown in Figure 7a. Extensive cracking and fracture of the matrix around the wear track represent direct microstructural evidence of thermal embrittlement of the matrix as a result of the repetitive freeze–thaw stresses introduced by the thermal cycling procedure. This leads to reduction of the load-bearing ability of the unreinforced polymer and its transition from ductile plowing toward brittle micro-cracking and fragmentation of the matrix material. In Figure 7e, the PLA + 10 wt% GF composite subjected to 400 thermal cycles is illustrated. It is evident that this sample possesses the most irregular groove morphology among all samples examined in the study: the plowing bands are wide, deep, and torn, possessing a jagged and splintered rim and loose angular fragments detached along the scar edges. The groove morphology of this sample is more disrupted than those of the aged pure PLA in Figure 7d and unaged 10 wt% composite in Figure 7b. The observed fiber-edge splintering and matrix tearing are explained by the degradation of the fiber–matrix interface due to the combination of thermal cycling and high-speed sliding. Namely, the mismatch in CTE between GFs and PLA matrix at this intermediate concentration of fibers results in interface debonding and fiber pull-out. Hence, the loosened

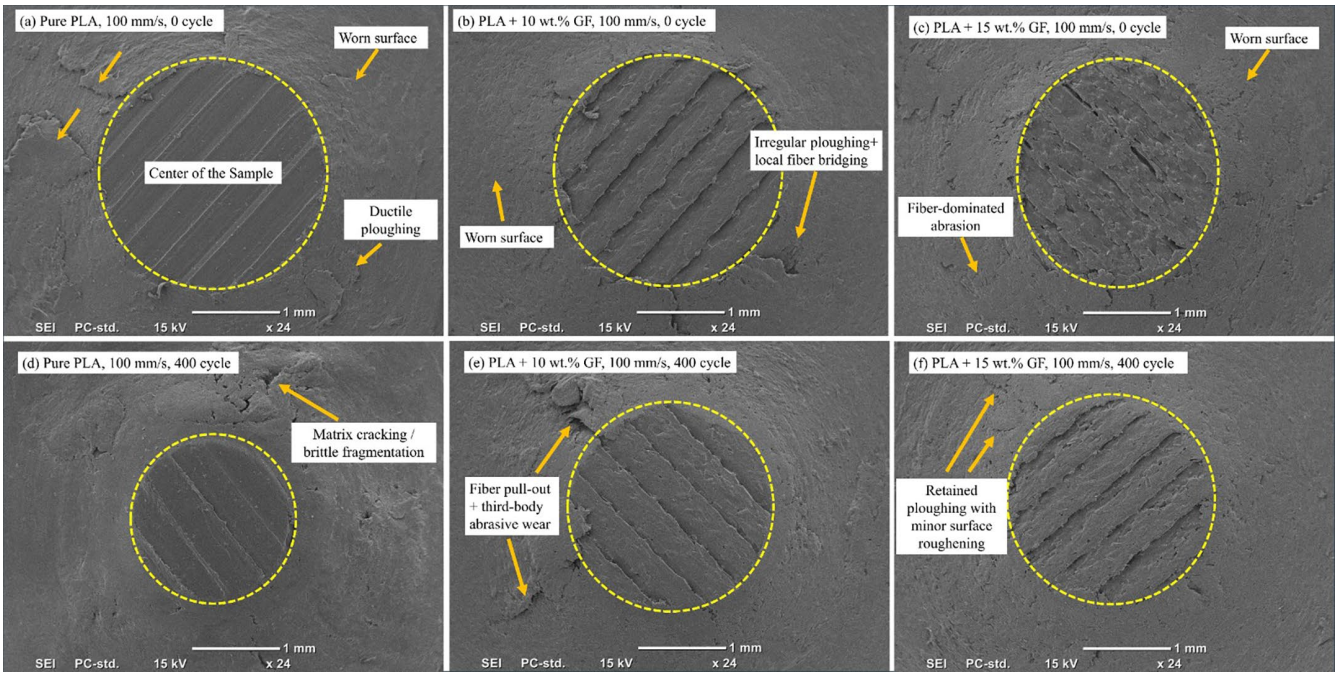

FIGURE 7 | SEM micrographs of ball-on-disk wear scars at 20 N load, 100 m track with a sliding speed of 100 mm/s: (a) pure PLA, 0 cycle; (b) PLA + 10 wt% GF, 0 cycle; (c) PLA + 15 wt% GF, 0 cycle; (d) pure PLA, 400 cycle; (e) PLA + 10 wt% GF, 400 cycle; (f) PLA + 15 wt% GF, 400 cycle.

15480569, 0, Downloaded from https://4spepublications.onlinelibrary.wiley.com/doi/10.1002/pc.71528 by Turkey Cochrane Evidence Aid, Wiley Online Library on [14/08/2026]. See the Terms and Conditions (https://onlinelibrary.wiley.com/terms-and-conditions) on Wiley Online Library for rules of use; OA articles are governed by the applicable Creative Commons License

fibers become trapped in the contact and act as third-body abrasive particles, increasing the material removal. This is consistent with the deepest wear track and the highest Sz profile value among all samples investigated. In Figure 7f, the PLA + 15 wt% GF composite subjected to 400 thermal cycles is illustrated. In this case, the wear scar remains comparatively confined and shows a distinguishable regular pattern of grooves, contrary to the torn pattern of the aged 10 wt% composite in Figure 7e. However, the groove edges are visibly rougher and more irregular than those of the unaged 15 wt% composite in Figure 7c. This relative preservation of the groove morphology is due to the fact that the higher and denser fiber concentration continues to provide an effective load-bearing skeleton even after maximum thermal cycling, thus restricting, though not completely preventing, the influence of thermal aging on the wear process.

In order to elucidate these damage modes in finer detail, the six wear scars were imaged once again, and the results are shown in Figure 8 below. Figure 8a confirms that the wear path of the unaged pure PLA exhibits zones of smeared, plastic deformation of the polymer matrix redeposited onto the groove track, proving that the plowing process visible at lower magnification is associated with localized adhesive material transfer instead of pure cutting. Figure 8b shows that the groove wear path of the unaged 10 wt% GF contains closely packed fine striations interspersed with fiber segments lying flat on the surface, confirming that the fibers are being plowed rather than dislodged. Figure 8c demonstrates that the unaged 15 wt% GF composite exhibits a more rugged, torn plateau-valley topology with elongated voids signifying localized fiber pull-out despite the shallow profile of this wear path, proving that some amount of pull-out does indeed take place in the highest-fiber concentration material prior to aging. Figure 8d presents the internal structure of the crack-bounded zone revealed in Figure 7d, featuring clusters of sharp edged micro-voids and fissures contained within a raised fragmented mound of the polymer matrix, thus verifying directly the embrittlement-induced mechanism of material detachment suggested previously by Figure 7d. Figure 8e displays a splintered angular debris fragment wedged between the torn boundary of the groove and scattered micro-voids on the bottom, thus supporting the accumulation of third-body debris consisting of detached fibers and matrix fragments. Figure 8f shows that the aged 15 wt% GF composite maintains a fine fibrous structure and only features some edge cracking without any of the detached material fragments observed in Figure 8e. Taken together, the series of images at higher magnifications reveals a sequence of increasing dominance of one damage mechanism over the other: from adhesive smearing and plowing of the unaged specimens, to the initial signs of fiber pull-out already detectable in the unaged 15 wt% GF composite, through embrittlement-induced micro-voiding in the aged pure PLA specimen, and finally, the generation of third-body debris due to fiber-edge splitting in the aged 10 wt% GF composite. Only the latter one remains immune to this effect, thus retaining a fibrous texture with very few voids and hence confirming its superior wear resistance.

The damage mechanisms revealed via SEM analysis coincide with the overall research literature on tribological properties of fiber-reinforced thermoplastic materials. In the case of unaged pure PLA material, the plowing with adhesive smearing mechanism that was detected correlates well with the experimental observations made by Zaghloul et al. [41] showing that unreinforced thermoplastics exhibit continuous ductile groove formation associated with plastic transfer of material during sliding against a counterface, which becomes increasingly

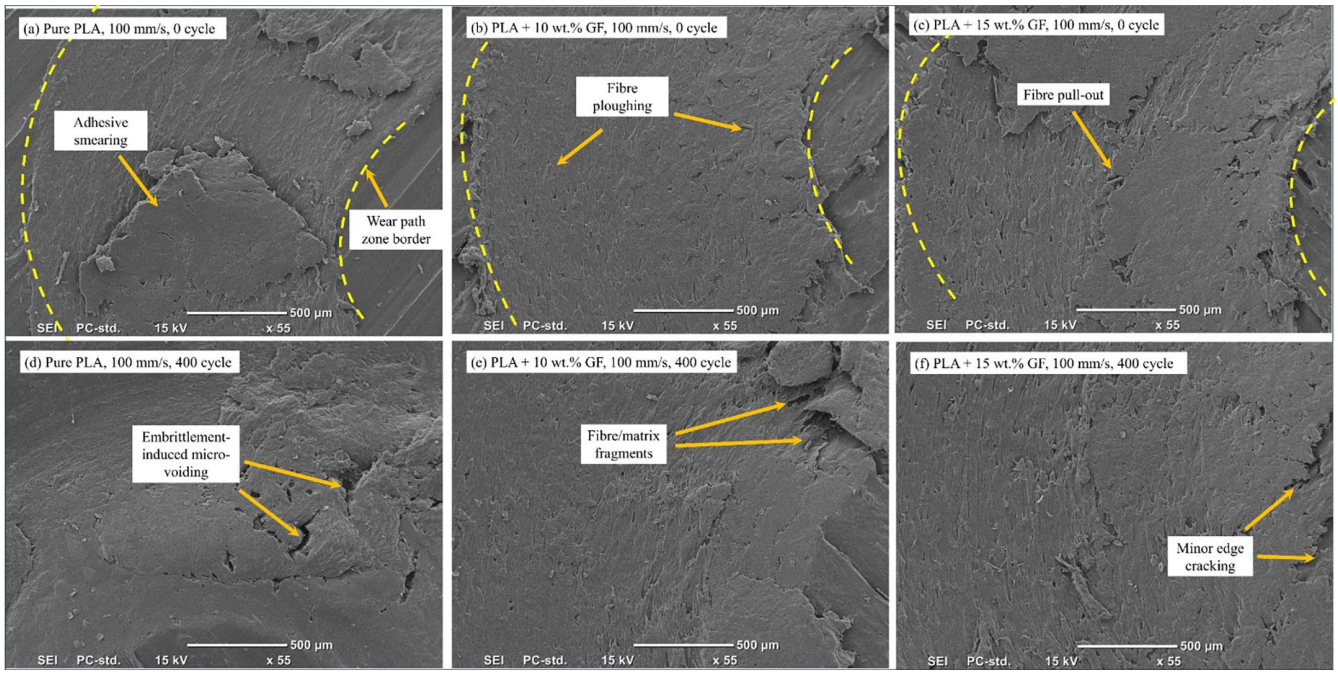

FIGURE 8 | Higher-magnification (×55) SEM micrographs of the ball-on-disk wear scars at 20 N load, 100 m track with a sliding speed of 100 mm/s: (a) pure PLA, 0 cycle; (b) PLA + 10 wt% GF, 0 cycle; (c) PLA + 15 wt% GF, 0 cycle; (d) pure PLA, 400 cycle; (e) PLA + 10 wt% GF, 400 cycle; (f) PLA + 15 wt% GF, 400 cycle.

15480569, 0, Downloaded from https://4spepublications.onlinelibrary.wiley.com/doi/10.1002/pc.71528 by Turkey Cochrane Evidence Aid, Wiley Online Library on [14/08/2026]. See the Terms and Conditions (https://onlinelibrary.wiley.com/terms-and-conditions) on Wiley Online Library for rules of use; OA articles are governed by the applicable Creative Commons License

TABLE 2 | Thermal transition temperatures and enthalpies of materials.

Sample code	T_g (°C)	T_c (°C)	T_m (°C)	ΔH_c (J/g)	ΔH_m (J/g)	$(X_c)_{rel}$ (%)
Pure PLA_0 cycles	59.47	97.06	151.54	26.78	31.71	100
Pure PLA_400 cycles	61.41	99.56	155.49	28.57	32.68	83.37
PLA + 10 wt% GF_0 cycles	62.56	99.59	150.70	24.57	27.88	74.60
PLA + 10 wt% GF_400 cycles	63.36	100.16	150.62	25.48	27.17	38.09
PLA + 15 wt% GF_0 cycles	62.82	99.03	149.04	20.30	25.93	134.35
PLA + 15 wt% GF_400 cycles	65.21	98.76	155.21	21.47	25.07	85.91

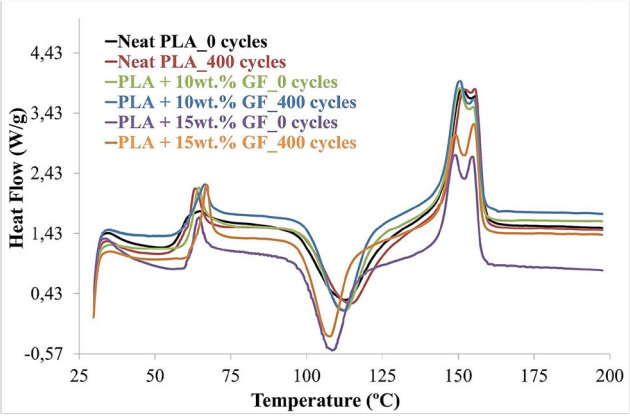

FIGURE 9 | DSC curves of pure PLA and GF-reinforced PLA composites before and after 400 thermal cycles.

suppressed by incorporation of rigid reinforcing particles. The transition to fiber-edge splintering, interfacial debonding, and generation of debris particles found in the aged 10 wt% GF composite are in line with the abrasive nature of tribological wear of GF-reinforced thermoplastics where fragments or protrusions of fibers get embedded into the sliding contact and act as hard abrasive particles that intensify wear rather than suppress it. The substantial matrix cracking and embrittlement observed in the thermally cycled pure PLA samples were corroborated by the results obtained by Huang et al. [42]. They reviewed that cycling between different temperatures leads to generation of residual stresses due to CTE mismatch between the stiff and dimensionally stable reinforcement and increasingly brittle and immobile matrix. Finally, the presence of voids and cracks in the FDM-printed PLA/GF composites in high magnifications coincides with the studies conducted by Dubey et al. [43] on additively manufactured short GF-reinforced PLA composites. They established that interlayer porosity and connected voids accelerate the process of microcracking and crack growth during cyclic loading, supporting the hypothesis about the preferential location of fiber pull-out and fragmentation in the preexisting voids.

3.4 | Differential Scanning Calorimetry Analysis

To study the effects of repeated thermal cycling on the thermal properties of the composite materials, DSC analysis was performed on the virgin materials (0 cycles) and on those that had undergone the maximum aging cycle (400 cycles), corresponding to the beginning and end of the thermal cycling. The DSC analysis was not used to determine the temperature at the contact interface created as a result of wear testing; the goal was rather to investigate changes in glass transition temperature, crystallization properties, and degree of crystallinity of the PLA matrix in relation to heat treatment. The fact is that there were no data regarding the contact temperature during wear, and hence it could not be considered an effect of frictional heating. The data on the thermal transition temperatures, enthalpies, and relative crystallinities ($X_{c,rel}$) of the prepared materials by DSC method are presented in Table 2. Moreover, the results of DSC thermograms of the material are shown in Figure 9.

From Table 2, it is seen that T_g of all composites increases with respect to pure PLA when GF is added. That is, T_g of pure PLA is 59.47°C, which becomes 62.56°C and 62.82°C when 10 and 15 wt% of GF are added, respectively. Moreover, it is seen that the value of T_g further increases in all the composites after 400 thermal cycles. This increase in the value of T_g of the samples with the addition of GF and after thermal cycling can be attributed to lower molecular mobility in the PLA matrix. It has been reported in the literature that RAF or the constrained amorphous interphase formed between crystalline and mobile amorphous regions of semicrystalline polymers can affect T_g due to restricted chain mobility, and that the structural relaxation in the amorphous region due to physical aging can increase T_g. Therefore, it can be assumed that the effect of the restricted chain mobility in the fiber–matrix interface due to GF addition and the structural changes in the amorphous region due to thermal cycling could have caused the increase in T_g [44–48].

As can be seen from Table 2, the ΔH_c values show a slight increase due to the thermal cycling of all samples under consideration. This means that despite the aging effect, all samples retain their ability to carry out the cold crystallization process during DSC heating. Cold crystallization is the reorganization of poorly ordered amorphous chains into the crystal structure during the heating process and is highly dependent on the structure of the amorphous phase. However, the decrease in $(X_c)_{rel}$ determined by using the proposed method in this work for all samples means that thermal cycling causes changes in the structure of the crystalline and amorphous phases. The largest decrease in $(X_c)_{rel}$ value is observed for composite with 10 wt% GFs, whereas composite with 15 wt% GFs that had the largest $(X_c)_{rel}$ value experiences an appreciable decrease after 400 cycles [44, 47, 49].

15480569, 0, Downloaded from https://4spepublications.onlinelibrary.wiley.com/doi/10.1002/pc.71528 by Turkey Cochrane Evidence Aid, Wiley Online Library on [14/08/2026]. See the Terms and Conditions (https://onlinelibrary.wiley.com/terms-and-conditions) on Wiley Online Library for rules of use; OA articles are governed by the applicable Creative Commons License

In conclusion, the DSC data confirm that thermal cycling caused changes in the structure of the PLA matrix and provide complementary information for the interpretation of the tribological properties. The increase in the values of T_g and the decrease in the values of $(X_c)_{rel}$ are indicative of the fact that thermal cycling causes changes in the polymer matrix structure and these changes correlate with the friction and wear characteristics described in the rest of the sections. In other words, the conclusions drawn indicate that tribological properties depend not only on the amount of GF but also on the microstructure changes caused by thermal cycling. In this context, the DSC results were used as complementary data for the interpretation of the cracking and brittle damage observed on the worn surfaces after thermal cycling. However, since the contact temperature was not measured during the wear tests, no direct relationship was established between the DSC results and friction-induced heating or thermal softening at the contact surface.

3.5 | Factorial Analysis

Factorial design refers to an experimentation method whereby various independent variables or factors can be changed at once in their various levels as opposed to the traditional way where they are evaluated one at a time. This type of experimental method is very crucial when designing engineering systems whose parameters interact as changing only one factor at a time without considering other factors would not bring out the effect of the interactions between the parameters. Using this factorial design provides for the assessment of each factor's combination making it easy to isolate the main and interaction effects.

Full-factorial design was chosen in favor of fractional factorial designs like Taguchi orthogonal arrays or BBD, based on the objectives of this investigation. Taguchi runs are usually used in robust parameter design, where higher-order interaction terms get confused with main effects or simply are not there—which is acceptable if interactions between factors are assumed to be negligible. In the current study, however, wear mechanisms turned out to be determined by strong coupling of factors, particularly Material × Sliding Rate and Sliding Rate × Thermal Cycle interaction. Using a Taguchi run would have meant confounding those interactions with the main effects and loss of an important result: the COF is determined by the interaction terms which account for 61.54% of the total variability. BBD was not considered for two reasons. The first one is that BBD is designed for continuous factors, where the second order response surface is fitted around the assumed optimum point. In our study, however, material composition is a categorical variable, rather than continuous. The second reason is that to cut down the number of experiments in BBD, the corners of factorial design are skipped, which is not acceptable in our case since the hierarchy reversal occurred under those extreme conditions, that is the combination of maximum shear velocity (100 mm/s) with maximum thermal aging (400 cycles). Due to the limited number of experimental runs (3 materials × 2 shear velocities × 3 aging levels = 18 treatment combinations), full-factorial design was still feasible in order to predict each effect as well as two- and three-way interaction. It was believed that such resolution was necessary in order to determine the causes of degradation and hierarchy reversal properly.

For this research work, the analysis of variance (ANOVA) technique was applied in order to calculate the proportion that each parameter contributes to the total variability in the obtained responses. Thus, the use of ANOVA in this research work has been for more than simply establishing any differences between different groups of experiments; it has been for determining the effect of each parameter involved.

In order to ensure that the statistics generated were reliable, each of the conditions used in the experiment was repeated three times to reduce any effects of random measurement error. The ANOVA was done on the complete data set using the replicate values for each condition and not just the means of the conditions. This allowed for an exact distinction between the two types of variation.

To systematically quantify the individual and interacting influences of material composition, sliding speed, and the number of thermal cycles on the wear-track depth (μm) of additively manufactured PLA composites, a general factorial regression analysis was executed based on the ANOVA compiled in Table S1. The established statistical model exhibits an exceptionally high coefficient of determination (R^2), with the model successfully accounting for 99.35% of the total variance in wear depth, leaving a minor, negligible experimental error component of just 0.65%. This extreme level of fit, combined with the highly significant overall model F-value of 321.72 ($p \leq 0.001$), firmly validates the statistical reliability and repeatability of the ball-on-disk configurations conducted on the replicated dataset. Among the primary independent variables, material composition emerged as the most dominant factor governing the wear depth, exhibiting a substantial percentage contribution of 34.67% accompanied by a commanding F-value of 954.42 ($p \leq 0.001$). This primary significance is deeply linked to the microstructural modifications induced by the GF reinforcement, where the rigid fibers possess significantly higher hardness and mechanical stiffness compared to the ductile polymer matrix, acting as primary load-bearing barriers that effectively anchor the surrounding matrix and restrict plastic deformation. Thermal cycling was identified as the second most influential main factor, yielding a percentage contribution of 17.69% and an F-value of 486.87 ($p \leq 0.001$). This highlights the severe susceptibility of additively manufactured composites to environmental aging stresses, where the severe mismatch in the CTE between the rigid GFs and the PLA matrix induces localized micro-voids, interfacial delamination, and matrix micro-cracking during freeze–thaw rounds that subsequently accelerate material removal via premature fiber peeling. In contrast, sliding speed independent of other variables showed a very low direct contribution of 0.73%, though it remained statistically significant due to its high F-value of 40.07 ($p \leq 0.001$), predominantly influencing the interface via frictional flash temperatures that cause localized matrix softening.

Besides the effects of individual factors, the interaction terms shown in Table S1 play an important role in elucidating the nonlinearity in wear, given that the set of two-way interactions together contribute to about 43.71% ($p \leq 0.001$) of the total variance. In particular, the Material × Sliding Speed interaction turned out to be the key term, contributing 28.36% ($F = 780.51$; $p \leq 0.001$). This means that an increase in sliding speed facilitates considerable plastic deformation and micro-grooving caused by simple matrix

15480569, 0, Downloaded from https://4spepublications.onlinelibrary.wiley.com/doi/10.1002/pc.71528 by Turkey Cochrane Evidence Aid, Wiley Online Library on [14/08/2026]. See the Terms and Conditions (https://onlinelibrary.wiley.com/terms-and-conditions) on Wiley Online Library for rules of use; OA articles are governed by the applicable Creative Commons License

softening of pure PLA, but in the case of GF composites, an increase in the sliding speed along with the formation of hard abrasive fiber debris may lead to very serious third-body wear regimes. Also, the interaction between Material and Thermal Cycling has proved to be statistically significant, accounting for 12.86% of variance ($F = 176.95$; $p \leq 0.001$). This confirms the fact that environment aging influences unfilled PLA and GF composites via completely different mechanisms because of the presence of fiber/matrix interfaces. Furthermore, the interaction between Sliding Speed and Thermal Cycling (contribution 2.50%; $F = 68.81$) and the 3-Way Material × Sliding Speed × Thermal Cycling interaction (2.55% of the variance; $F = 35.03$) have been highly significant ($p \leq 0.001$). Therefore, the significance of such high-order interactions highlights the fact that in engineering practice, the final wear depth of these FDM-printed components depends on a combined mechanism, in which the thermally induced micro-cracks are linked to frictional heating depending on speed and anchoring capacity of material.

As can be seen from the major effect plots of wear depth presented in Figure S1, these results clearly demonstrate the physical realization of the contradictory regimes of wear and degradation on the tribological interface of the FDM composites by the mechanisms of micro-mechanics and heat generation. In this case, for the pure PLA samples, the clear tendency toward a significant growth in the mean wear depth for pronounced temperature cycling, rounds, and high sliding speeds demonstrates the vulnerability of the base material toward the processes of environmental aging and local heating due to friction. The periodic changes in the freezing–melting conditions lead to the cyclic changes in the volume of the unreinforced polymer that destabilizes its molecular structure, while the continuous mechanical action on it causes thermal softening. However, in turn, the considerable and steady decline in the wear depth for 10 and 15 wt% GF shows the clear evidence of the ability of the fibers to act as the rigid support structures. In this case, due to the incorporation of the stiff microstructures into the PLA composite, the penetration of the 100Cr6 (AISI 52100) steel ball is limited by the resistance of the fibers to the normal force.

An in-depth look at structural gradients as a function of factor levels provides deeper insights into the non-linear cross-over effects that are supported by significant interaction factors in the ANOVA analysis. While sliding speed does play a minor role in influencing material wear directly, the effect becomes significantly noticeable when it is viewed in combination with material condition, thus demonstrating the physical significance of the material × sliding speed interaction. For example, in case of pure PLA, increased sliding speeds cause viscous deformation of the material due to flash temperature formation near the surface of the specimen. At the same time, GF reinforced PLA is subject to a completely different damage mechanism since the thermal softening of the material interacts with the GF network structure. After being exposed to maximum environmental conditions (400 thermal cycles), the difference in CTE between GFs and PLA causes development of micro-boundary debonding, cluster of micro-voids and macro cracks at FDM track layer interfaces. Further mechanical stress caused by sliding at high sliding speeds leads to fiber separation and destruction because the weakened interfaces cannot withstand such stresses. Rigid glass fragments become incorporated into the wear process resulting in transition from plastic shearing wear to third body abrasion regime and changes in wear morphology. Thus, the lines in Figure S1 show that wear-depth progression occurs as a result of a synergic effect of multiple factors where the interaction of micro-crack formation and frictional heating at high speed occurs.

In order to evaluate quantitatively the individual and combined influences of the material composition, the sliding velocity, and the number of thermal cycles on the wear-track width (μm) of the additively manufactured PLA composites, an overall factorial regression model was obtained using the ANOVA data from Table S2. This statistical model demonstrates a high coefficient of determination (R^2) of 97.61%, where 2.39% corresponds to experimental error. Such a high degree of fit, along with an important significance (F-value = 86.41; $p \leq 0.001$) of the whole regression model, confirms that the chosen approach describes the wear process quite accurately. Unlike the previous wear depth analysis, there is a dominant combination of the main independent variables affecting track width, where the sliding velocity accounts for 23.12% ($F = 347.95$; $p \leq 0.001$), the number of thermal cycles accounts for 22.58% ($F = 169.89$; $p \leq 0.001$), and the material composition accounts for 14.48% ($F = 108.93$; $p \leq 0.001$). Such a high direct influence of the sliding velocity on the width of the track confirms the increase in lateral wear due to higher kinetic velocities, meaning that as the counterface ball slides faster, the local flash temperatures increase faster in contact asperities leading to near-surface plastic flow and macro-grooving and thus widening the borders of the track. At the same time, hydrothermal stress alternation cycles (0 to 400) systematically weaken the border regions of the FDM track layers due to volume expansion and formation of micro-cracks in freezing stages, and thus facilitate edge breaking during mechanical sliding. The material composition as the rigid GF skeletal network is the main limiting factor that prevents lateral plowing due to anchorage of the ductile PLA matrix and thus leaves the total linear contributions equal to 60.17%.

In addition to the independent factors, the interaction effects in Table S2 clearly illustrate the extremely complex relationships between wear mechanisms, with two-way and three-way interactions being responsible for 37.44% of the total variance ($p \leq 0.001$). The interaction effect Material × Sliding Speed was identified as the most important interaction effect, explaining 19.99% of the total variation in data ($F = 150.39$, $p \leq 0.001$). Thus, whereas sliding speed increases the rate of widening of the pure PLA due to thermal softening and viscous flow, the interaction with GF materials causes a transition into abrasive wear regime. At higher sliding speeds, shear forces rapidly break off and fragment the rigid glass particles which then get entrained as abrasive third body particles causing significant lateral expansion of the wear trace relative to that of the base polymer. The interaction effect Sliding Speed × Thermal Cycling explains 6.63% of the total variance ($F = 49.91$, $p \leq 0.001$) and Material × Thermal Cycling explains 4.72% of the total variance ($F = 17.75$, $p \leq 0.001$), thus showing that aging conditions make structural interfaces vulnerable to the speed-dependent thermal degradation and specific material delamination. Finally, the statistically highly significant interaction effect Material × Sliding Speed × Thermal Cycling explains 6.10% of the total variance ($F = 22.59$, $p \leq 0.001$) and

15480569, 0, Downloaded from https://4spepublications.onlinelibrary.wiley.com/doi/10.1002/pc.71528 by Turkey Cochrane Evidence Aid, Wiley Online Library on [14/08/2026]. See the Terms and Conditions (https://onlinelibrary.wiley.com/terms-and-conditions) on Wiley Online Library for rules of use; OA articles are governed by the applicable Creative Commons License

proves that the process of widening the wear scar width is a complex synergetic process, during which thermally created interfacial cracks cooperate with the speed-dependent frictional heating and matrix anchorage limitation.

The main effects plots for the wear-track width, which are illustrated in Figure S2 below, serve as a physical illustration of how the lateral deformation behavior of FDM-printed PLA-based composite systems is determined by common parametric influence, separate from the patterns observed in the wear depth parameter. In perfect harmony with the multifactor ANOVA data presented in Table S2 above, the graphs present a monotonically increasing wear scar width in response to rising sliding speed values and advancing thermal aging cycles. In the pure PLA samples, the pronounced upward trend along the sliding speed axis corresponds to the fast accumulation of near-surface frictional flash temperatures caused by the interacting asperities. The fast thermal rise leads to the viscoelastic flow formation, which allows for the lateral outflow of the ductile polymer tracks in response to the plowing effect of the counter-face ball. Meanwhile, the environmental exposure accumulated over 0–400 thermal cycles gradually degrades the track edges in the composite specimens. The volumetric stresses formed by the condensation and subsequent freezing of the water content cause micro void clustering and sequential delamination of the layers in the FDM-based composite tracks. This hydrothermal degradation significantly decreases the cohesion of the matrix, making the mechanical shear forces capable of fracturing the unsupported edges of the wear track more easily, thus widening the width of the resulting scar on the macro-level.

As a result of the analysis of the direction of change and variation of the slopes at different factor levels, it can be concluded that the highly significant interaction terms, including the Material × Sliding Speed term, which explains 19.99% of total variance, have a physical justification. Assuming that the two control parameters acted independently from each other, the upward trend in the case of the increasing sliding speed would be consistent regardless of the material type; instead, the variation of the slopes shows the increased rate of change in wear mechanism. In the unreinforced PLA matrix, the increased velocities simply contribute to the acceleration of the viscous deformation and thermal softening. On the contrary, in the case of 10 and 15 wt% GF reinforced formulations, the combination of the environmentally degraded, brittle interfaces and fast shear at high speeds causes the emergence of a third-body abrasive configuration. The continuous mechanical shearing at high sliding speeds dislocates the debonded, due to the CTE mismatch, GFs and entraps them into the steel ball as abrasive agents, micro-cutting the lateral edges of the wear channel. As a result, the parametric graph in Figure S2 proves that the horizontal expansion of the wear track is not a simple result of independent variables' impact, but a synergetic phenomenon in which the hydrothermally damaged interfaces, speed-dependent frictional softening, and fiber anchoring threshold are continuously overlapping.

In order to quantify the effects of the material composition, sliding speed, and thermal cycling on the average COF of PLA-based AM composites through an integrated analysis approach, the factorial regression of general form on the basis of ANOVA of Table S3 was carried out. The obtained statistical model possesses a high coefficient of determination (R^2), accounting for 89.24% of the total variance in the friction coefficient, with the experimentally controlled error term taking 10.76% share of the total variance. High fit level and statistically highly significant overall F-value of the model ($F = 17.56$, $p \leq 0.001$) confirm its statistical reliability. In comparison with linear dominant influence observed for the wear depth and width, the friction behavior is dominated by interaction effects, since the 2-Way and 3-Way interactions in total explain 61.54% of the total variance in COF. On the other hand, the share of linear effects of the main factors takes only 27.69% of the total variance, including: Sliding Speed (12.77%, $F = 42.73$, $p \leq 0.001$), Material Composition (8.42%, $F = 14.09$, $p \leq 0.001$), and Thermal Cycling (6.50%, $F = 10.87$, $p \leq 0.001$). Such structure of factors' effects shows that the COF is determined not only by the material property but is mainly a function of the system response, since the effect of increased sliding speed changes the shear rate and frictional flash temperatures of asperities while the GF network and hydrothermal aging change the interface deformation and the distribution of shear stresses.

It is clear that the tribological interface possesses a highly complex and coupled nature, based on the prevalence of higher-order terms in Table S3. The interaction of Sliding Speed and Thermal Cycling (2-way) reveals itself to be the critical driving parameter, making up a considerable 20.77% of variance with F-value of 34.75 ($p \leq 0.001$). This implies that the velocity-dependent friction process demonstrates a highly noticeable change in its behavior depending on the environmental degradation experience of the FDM parts. With the thermal aging, hydrothermal cycles produce cracks and relaxation of the interface in PLA; during the increasing sliding speed, these weakened layer structures change the real contact area, which leads to the acceleration of the adhesive stick–slip or debris production processes responsible for friction coefficient changes. Furthermore, the three-way interaction between Material × Sliding Speed × Thermal Cycling explains a considerable 23.36% of variance, with F-value of 19.54 ($p \leq 0.001$). Such highly significant three-factor interaction gives mathematical proof to the existence of "decoupling effect" between the material loss and friction mechanism. With the thermal stresses acting on aged samples with 10 and 15 wt% GF, the fiber–matrix interfaces experience the mismatching of CTE values, leading to the disruption of these interfaces. High speed of the sliding produces fiber pull-out and breaking from these disrupted interfaces, creating loose rigid glass particles in the contact zone. Such detached fibers behave as abrasive third bodies that produce the lateral plowing of the interface, creating a highly resisting abrasive sliding mode in which the COF can increase drastically; sometimes even exceed one; even while maintaining the stability of volumetric wear due to matrix reinforcement. In conclusion, the significance of the interaction parameters demonstrates that the friction behavior of the FDM-printed composites under real environment conditions is a complex nonlinear system in which the synergy of environment-induced micro-cracking and velocity-induced thermal softening and debris evolution plays a crucial role.

The major plots of the mean COF, as presented in Figure S3, demonstrate an evident physical manifestation of the complicated and highly coupled nature of the interfacial processes happening within the tribological contact interface. In contrast to

15480569, 0, Downloaded from https://4spepublications.onlinelibrary.wiley.com/doi/10.1002/pc.71528 by Turkey Cochrane Evidence Aid, Wiley Online Library on [14/08/2026]. See the Terms and Conditions (https://onlinelibrary.wiley.com/terms-and-conditions) on Wiley Online Library for rules of use; OA articles are governed by the applicable Creative Commons License

the wear-track parameters, in which the linear factor behavior is primarily prevailing, the dynamic COF profiles contain non-monotonous transitions and significant dependency on the coupled parameter values. For the reference samples of pure PLA, the variations of the mean COF with respect to the sliding velocity are determined by the balance of two contradicting factors: the shear-rate increase and the accumulation of the friction flash heat, which leads to a transient viscoelastic stick–slip regime. With the increasing GF content (10 and 15 wt%), the initial baseline friction curves are changed in structure. High stiffness micro-fibers, while stabilizing the depth of the wear track, operate as hard asperities which interfere with the sliding process and change the friction profiles to the rough-micro-abrasion regime.

A deeper analysis of trends in relation to the environmental factor levels highlights the physical effects associated with multiple interactions, especially with regard to the very dominant effect of Sliding Speed × Thermal Cycling (20.77%) and the 3-Way interaction of Material × Sliding Speed × Thermal Cycling (23.36%) effects based on ANOVA test. As a result of the significant exposure of the composites to various environmental conditions to reach up to 400 thermal cycling effects, there is a noticeable discrepancy in the CTE between GFs and PLA matrix that results in the disruption of the bonding interfaces. With the following sliding tests under higher speeds, such thermally weakened interfaces will fail to hold the cohesion of the reinforcement material leading to premature pull-out and disintegration of the fibers. In other words, the loose and disintegrated rigid GFs get trapped with the counterface ball creating an abrasive third body rather than the traditional two-body sliding. This aggressive third-body abrasive mechanism significantly contributes to increased mechanical resistance that leads to a considerable increase in the COF to the point of exceeding the value of unity while the actual volumetric loss of the materials stays low because of the skeletal shielding of the fibers. Hence, the trends demonstrated in Figure S3 illustrate an important "friction-wear dissociation" effect whereby the dynamic COF is a very sensitive system variable defined by the synergy of environmental micro-cracking, velocity-related thermal softening, and wear particle generation processes.

The following per-unit (p.u.) radar chart in Figure S4 allows us to make a unified and comprehensive study of the cumulative influence of the composition, sliding speed and thermal cycling aging on the tribological performance signatures of FDM-printed PLA-based composites. The aforementioned mathematical tool gives us the evidence for the dominant mechanisms that have been found in the above-mentioned multifactor ANOVA (Tables S1–S3). One of the most important features in Figure S4 is the coordinated increase of wear-track depth (red), wear width (blue), and COF (green) in relation to increased aging severity from 0 to 400 thermal cycling and increase of sliding velocity from 50 to 100 mm/s. The high-order interactions in particular 3-Way Material × Sliding Speed × Thermal Cycling are justified from the physical point of view. During maximum environmental aging (400 cycles), the significant difference between the coefficient of thermal expansion (CTE) leads to failure of the interface between matrix and fibers. As soon as the materials start sliding at high speed under such damaged interfaces, catastrophic failure of the fibers occurs and they become debonded and fragmented. Consequently, the system moves into the regime of severe abrasive wear caused by third body particles. Increase of all three metrics in Figure S4 means the failure of the protective microstructure. Taken together, Figure S4 makes it possible to state empirically that engineering lifetime estimation of additively manufactured parts cannot be made through the consideration of some simple isolated factors. Figure S4 proves that the engineering lifetime is controlled by the ecosystem wherein micro-cracks formation and thermally activated velocity dependent softening interact consistently to control the tribological behavior.

4 | Conclusions

This work examines the combined effects of thermal cycling aging and amount of milled GF filler on tribological properties of FDM-printed PLA composites using methods of friction tests, 3D optical profilometry, SEM, differential scanning calorimetry, and full-factorial ANOVA. Main findings are outlined below.

At a relatively low sliding speed of 50 mm/s, GF reinforcement demonstrated a monotonous protective hierarchy irrespective of aging state. The composite containing 15 wt% of GFs had the shallowest and narrowest wear tracks under all considered conditions reaching the maximal wear depth only 81 μm after 400 thermal cycles, as compared with 217 μm for pure PLA. It can be explained by the skeleton effect of the fiber network.

Thermal cycling aging provoked a significant embrittlement of the unreinforced PLA matrix. Pure PLA after 400 cycles had well-developed networks of peripheral cracks, crater-like morphologies, and near doubling of the maximal peak-to-valley height (Sz: 287.6; 567.1 μm), which points out the transition of wearing mechanism from ductile abrasive plowing to brittle fracture and delamination-induced wear.

Under high sliding speed (100 mm/s) and the highest aging (400 cycles) level, the reinforcement hierarchy was destroyed and inverted. The interphase debonding owing to CTE mismatch caused fiber pull-out and formation of an abrasive environment of rigid glass fragments. It resulted in the appearance of severe third body abrasion mode, leading to the deepest wear scar in aged 10 wt% GF composite (209 μm; Sz = 716.5 μm), compared to even aged pure PLA.

The DSC analysis confirmed changes in the microstructure of the specimens, namely, an increase in the glass transition temperature and reduction in the relative degree of crystallinity after 400 cycles, which points out limited mobility of chains and amorphous phase structure modification. These changes were consistent with the observed degradation of the tribological performance of the samples. However, the DSC results were used only as complementary data to characterize the changes caused by thermal cycling and were not considered as direct evidence of friction-induced heating or thermal softening during the wear tests.

Factorial ANOVA revealed that the main factor for the wear depth was the material composition (34.67%), the sliding speed determined the wear-track width (23.12%), and the influence of the higher-order interaction was the main factor affecting the

15480569, 0, Downloaded from https://4spepublications.onlinelibrary.wiley.com/doi/10.1002/pc.71528 by Turkey Cochrane Evidence Aid, Wiley Online Library on [14/08/2026]. See the Terms and Conditions (https://onlinelibrary.wiley.com/terms-and-conditions) on Wiley Online Library for rules of use; OA articles are governed by the applicable Creative Commons License

friction coefficient (61.54%), where the three-factor Material × Sliding Speed × Thermal Cycling term contributed by 23.36%. Thus, the results demonstrate that the tribological response comes from the interaction of system parameters.

In conclusion, it can be stated that reinforcement content cannot be selected independently of service environment: the most efficient reinforcement of 15 wt% GF provides robust protection in low-speed conditions even after significant aging, but simultaneous presence of high sliding speed and thermal cycling represents the critical regime where the advantages of fiber reinforcement disappear.

Further research must include extending the thermal cycle up to more than 400 cycles so as to establish whether the reported hierarchy inversion effect occurring at very high sliding velocities represents a temporary or permanent degradation phase. In addition, further work needs to be done in investigating the effect of different levels of GF inclusion as well as other fiber configurations (such as continuous fiber or woven fiber configurations) so as to establish the ideal level of fiber inclusion which combines low-speed damage resistance and high-speed abrasion resistance. In addition, future studies must include post-test analysis of the counterface by scanning electron microscopy combined with energy-dispersive spectroscopy (SEM/EDS) of the 100Cr6 ball surface and elemental distribution within the wear scars. Such analysis will help to estimate the thickness and stability of the transferred polymer film, the presence of which can now be confirmed only on the basis of friction measurements and specimen morphological characteristics. Finally, linking the experimental thermal cycle and wear performance of the laboratory scale with actual environmental exposure and loading would improve the practical significance of these results for applications of PLA composites in aerospace and outdoor environments.

Author Contributions

Sinan Fidan: conceptualization, investigation. **Satılmış Ürgün:** validation, software. **Nevin Gamze Karsli:** investigation, writing – review and editing. **Taner Yilmaz:** conceptualization, investigation, visualization. **Mustafa Özgür Bora:** methodology, software, data curation. **Mehmet İskender Özsoy:** writing – review and editing, investigation.

Funding

In this study, the material manufacturing process was funded by the Kocaeli University Scientific Research Projects Coordination Unit [Project no: FBA-2025-4756].

Conflicts of Interest

The authors declare no conflicts of interest.

Data Availability Statement

The data that support the findings of this study are available from the corresponding author upon reasonable request.

References

1. M. A. Islam, M. H. Mobarak, M. I. H. Rimon, et al., "Additive Manufacturing in Polymer Research: Advances, Synthesis, and Applications," *Polymer Testing* 132 (2024): 108364, https://doi.org/10.1016/j.polymertesting.2024.108364.

2. T. A. Yeshiwas, A. B. Tiruneh, and M. A. Sisay, "A Review Article on the Assessment of Additive Manufacturing," *Journal of Materials Science: Materials in Engineering* 20 (2025): 85, https://doi.org/10.1186/s40712-025-00306-8.

3. R. Kumar, H. Mehdi, S. S. Bhati, M. Arunkumar, S. Mishra, and M. K. Lohumi, "A Comprehensive Review of Advancements in Additive Manufacturing for 3D Printed Medical Components Using Diverse Materials," *Discover Materials* 5 (2025): 152, https://doi.org/10.1007/s43939-025-00349-w.

4. E. H. Tümer and H. Y. Erbil, "Extrusion-Based 3D Printing Applications of PLA Composites: A Review," *Coatings* 11 (2021): 390, https://doi.org/10.3390/coatings11040390.

5. N. A. A. B. Taib, M. R. Rahman, D. Huda, et al., "A Review on Poly Lactic Acid (PLA) as a Biodegradable Polymer," *Polymer Bulletin* 80 (2023): 1179–1213, https://doi.org/10.1007/s00289-022-04160-y.

6. X. Zhao, L. Liang, F. Mo, et al., "Environment Friendly, Renewable and Sustainable Natural Fiber-Reinforced Polylactic Acid (PLA) Composites," *Polymer Composites* 47 (2026): S9–S36, https://doi.org/10.1002/pc.70796.

7. J. Santo, V. Pradhik, S. Kalakoti, P. Saravanan, and P. K. Penumakala, "Effect of Composite Processing Technique on Tribological Properties of 3D Printed PLA-Graphene Composites," *Tribology International* 198 (2024): 109895, https://doi.org/10.1016/j.triboint.2024.109895.

8. A. Nassar, G. E. Abouseriaa, A. Alshorbagy, M. Megahed, and E. Nassar, "Effect of Infill Parameters and Thermal Annealing on the Mechanical Behavior of FDM 3D-Printed Polymer," *Scientific Reports* 16 (2026): 18166, https://doi.org/10.1038/s41598-026-54969-0.

9. Ç. Bolat, F. Demircan, İ. Gür, B. Yalçın, R. Şener, and A. Ercetin, "Hardness and Surface Roughness of 3D-Printed ASA Components Subjected to Acetone Vapor Treatment and Different Production Variables: A Multi-Estimation Work via Machine Learning and Deep Learning," *Polymers* 17 (2025): 2881, https://doi.org/10.3390/polym17212881.

10. Ç. Bolat, B. Ergene, and H. Ispartalı, "A Comparative Analysis of the Effect of Post Production Treatments and Layer Thickness on Tensile and Impact Properties of Additively Manufactured Polymers," *International Polymer Processing* 38 (2023): 244–256, https://doi.org/10.1515/ipp-2022-4267.

11. M. Kočiško, L. Štafura, K. Goryl, and Z. Mitaľová, "Evaluation of the Effect of Post-Processing Methods on the Surface Parameters of Parts Produced by FFF/FDM Technology," *Materials* 18 (2025): 4672, https://doi.org/10.3390/ma18204672.

12. Y. S. Ahmed, N. Ankah, C. Ayranci, and F. Alam, "Additive Manufactured Sandwich Structures for Enhanced Mechanical and Thermal Performance of PLA/Carbon Fiber Composites," *Composites Part A, Applied Science and Manufacturing* 209 (2026): 109947, https://doi.org/10.1016/j.compositesa.2026.109947.

13. P. Jagadeesh, S. M. Rangappa, S. Rangappa, C. Anilkumar, P. Kalappa, and S. Siengchin, "Effect of Infill Pattern and Filler Ratio on the Mechanical Properties of 3D Printed Eco-Friendly Wollastonite/Polylactic Acid Composites," *Journal of Thermoplastic Composite Materials* 39 (2026): 292–322, https://doi.org/10.1177/08927057251344247.

14. R. Ozah, J. V. S. P. Kumar, S. H. Anand, and C. R. Kumar, "Experimental Investigation on Mechanical, Flammability, Wear and Thermal Properties of 3D Printed Polylactic Acid Composite Containing Rice Husk Ash/Si_3N_4 Nanoparticles," *Journal of the Australian Ceramic Society* 61 (2025): 1211–1222, https://doi.org/10.1007/s41779-025-01154-7.

15. K. Vishal, K. Rajkumar, P. Sabarinathan, and V. Dhinakaran, "Mechanical and Wear Characteristics Investigation on 3D Printed Silicon Filled Poly (Lactic Acid) Biopolymer Composite Fabricated by Fused

15480569, 0, Downloaded from https://4spepublications.onlinelibrary.wiley.com/doi/10.1002/pc.71528 by Turkey Cochrane Evidence Aid, Wiley Online Library on [14/08/2026]. See the Terms and Conditions (https://onlinelibrary.wiley.com/terms-and-conditions) on Wiley Online Library for rules of use; OA articles are governed by the applicable Creative Commons License

Deposition Modeling," *Silicon* 14 (2022): 9379–9391, https://doi.org/10.1007/s12633-022-01712-9.

16. S. A. Abed, A. M. K. Al-Khafaji, and M. M. Hanon, "Enhancement of Wear Resistance in 3D-Printed PLA and CF-PLA/Epoxy Composites via Taguchi Design and ANOVA," *Tribology in Industry* 47 (2025): 1–9, https://doi.org/10.24874/ti.1992.07.25.09.

17. G. Lasch, G. G. Sostizzo, G. S. Gehlen, et al., "Exploring the Tribological Properties of 3D Printed Polymer Composites: An Experimental Study," *Polymer Composites* 47 (2026): 6840–6858, https://doi.org/10.1002/pc.70591.

18. Y. Kaplan, "Tribological Performance of Additively Manufactured Tungsten-Reinforced PLA Composites," *Afyon Kocatepe University Journal of Sciences and Engineering* 26 (2026): 489–496, https://doi.org/10.35414/akufemubid.1776539.

19. R. Tyagi, N. Ranjan, M. Kumar, V. Kumar, A. Tripathi, and R. Kumar, "Investigation of Wettability and Wear Properties on 3D Printed Polylactic Acid/Molybdenum Disulfide–Silicon Carbide Polymeric Composite for Sustainable Biomedical Applications," *Journal of Thermoplastic Composite Materials* 38 (2025): 93–114, https://doi.org/10.1177/08927057241243356.

20. M. Selwin, R. Nagarajan, S. Ponsuriyaprakash, N. Ayrilmis, K. Krishnan, and F. Mohammad, "Optimization of Wear Behavior of Additively Manufactured Green Biocomposites From Printed Polylactic Acid (PLA) and Microcrystalline Cellulose," *Wood Material Science & Engineering* 21 (2026): 1051–1060, https://doi.org/10.1080/17480272.2025.2466226.

21. P. P. Parlevliet, H. E. N. Bersee, and A. Beukers, "Residual Stresses in Thermoplastic Composites-A Study of the Literature-Part I: Formation of Residual Stresses," *Composites Part A: Applied Science and Manufacturing* 37 (2006): 1847–1857, https://doi.org/10.1016/j.compositesa.2005.12.025.

22. R. Acharya and V. M. Karbhari, "Effect of Elevated Temperature Thermal Aging/Exposure on Shear Response of FRP Composites: A Topical Review," *Polymers* 18 (2026): 354, https://doi.org/10.3390/polym18030354.

23. I. I. Muna, M. Mieloszyk, R. Rimasauskiene, N. Maqsood, and M. Rimasauskas, "Thermal Effects on Mechanical Strength of Additive Manufactured CFRP Composites at Stable and Cyclic Temperature," *Polymers* 14 (2022): 4680, https://doi.org/10.3390/polym14214680.

24. S. Mahdavi, S. K. Gupta, and M. Hojjati, "Thermal Cycling of Composite Laminates Made of Out-Of-Autoclave Materials," *Science and Engineering of Composite Materials* 25 (2018): 1145–1156, https://doi.org/10.1515/secm-2017-0132.

25. S. M. R. Khalili, M. Najafi, and R. Eslami-Farsani, "Effect of Thermal Cycling on the Tensile Behavior of Polymer Composites Reinforced by Basalt and Carbon Fibers," *Mechanics of Composite Materials* 52 (2017): 807–816, https://doi.org/10.1007/s11029-017-9632-5.

26. G. M. Sicoe, A. Dorbane, and D. C. Anghel, "Exploring the Effects of Thermal Cycling on the Precision of 3D-Printed Parts: A Comprehensive Analysis," *Applied Sciences* 15 (2025): 12955, https://doi.org/10.3390/app152412955.

27. H. Xu, J. Chen, Y. Lu, et al., "Effect of Accelerated Aging on the Performances of 3D Printed Polylactic Acid-Polyhydroxyalkanoate Specimens," *Polymer Engineering and Science* 66 (2026): 6137–6149, https://doi.org/10.1002/pen.70654.

28. M. R. Khosravani and T. Reinicke, "Effects of Geometry and Thermal Aging on the Strength of 3D-Printed Polymer Parts," *Procedia Structural Integrity* 53 (2024): 264–269, https://doi.org/10.1016/j.prostr.2024.01.032.

29. Y. H. Liow, K. I. Ismail, and T. C. Yap, "Tribology Behavior of In-Situ FDM 3D Printed Glass Fibre-Reinforced Thermoplastic Composites," *Journal of Research Updates in Polymer Science* 13 (2024): 86–93, https://doi.org/10.6000/1929-5995.2024.13.10.

30. L. Palaniandy, K. I. Ismail, and T. C. Yap, "Tribological Behaviour of 3D Printed Polylactic Acid (PLA) Sliding Against Steel at Different Sliding Speed," *Journal of Physics: Conference Series* 2542 (2023): 12003, https://doi.org/10.1088/1742-6596/2542/1/012003.

31. R. Autay, A. Njeh, and F. Dammak, "Effect of Hygrothermal Aging on Mechanical and Tribological Behaviors of Short Glass-Fiber-Reinforced PA66," *Journal of Thermoplastic Composite Materials* 32 (2019): 1585–1600, https://doi.org/10.1177/0892705718796554.

32. A. E. Sahin, E. Yarar, H. Kara, E. B. Cep, M. O. Bora, and T. Yilmaz, "Thermal Aging Effect of Polyamide 6 Matrix Composites Produced by Tailor Fiber Placement (TFP) Under Compression Molding on Sliding Wear Properties," *Polymer Composites* 45 (2024): 98–110, https://doi.org/10.1002/pc.27466.

33. C. Birleanu, M. Cioaza, F. Serdean, M. Pustan, P. Bere, and G. Contiu, "Tribological Investigation of Glass Fiber Reinforced Polymer Composites Against 52100 Chrome Alloy Steel Based on ELECTRE Decision-Making Method," *Polymers* 16 (2024): 62, https://doi.org/10.3390/polym16010062.

34. S. Fidan, S. Ürgün, M. İ. Özsoy, M. Ö. Bora, and E. Güleç, "Tribological Response of Glass Fiber/Polyester Composites After Pressurized Water-Immersion Aging Assessed by Reciprocating and Ball-On-Disc Wear Testing," *Polymers* 17 (2025): 2503, https://doi.org/10.3390/polym17182503.

35. S. Yilmaz, O. Gul, B. Eyri, N. G. Karsli, and T. Yilmaz, "Analyzing the Influence of Multimaterial 3D Printing and Postprocessing on Mechanical and Tribological Characteristics," *Macromolecular Materials and Engineering* 309 (2024): 2300428, https://doi.org/10.1002/mame.202300428.

36. S. Fidan, S. Ürgün, N. G. Karsli, T. Yilmaz, M. Ö. Bora, and M. İ. Özsoy, "Effects of Pressurized Water Aging on Reciprocating Friction and Wear of FDM 3D-Printed PLA and Glass Fiber Reinforced PLA Composites," *Polymers* 18 (2026): 406, https://doi.org/10.3390/polym18030406.

37. B. Ergene and Ç. Bolat, "An Experimental Study on the Role of Manufacturing Parameters on the Dry Sliding Wear Performance of Additively Manufactured PETG," *International Polymer Processing* 37 (2022): 255–270, https://doi.org/10.1515/ipp-2022-0015.

38. A. Phogat, D. Chhabra, V. Sindhu, and A. Ahlawat, "Analysis of Wear Assessment of FDM Printed Specimens With PLA, Multi-Material and ABS via Hybrid Algorithms," *Materials Today: Proceedings* 62 (2022): 37–43, https://doi.org/10.1016/j.matpr.2022.01.429.

39. Ç. Bolat and E. Yıldırım, "A Comparative Effort on the Influence of Liquid Treatment Media Type, Fiber Addition, and Deformation Load on the Wear Performance of Additively Manufactured Polyamide 6 and Acrylonitrile Butadiene Styrene Composites," *Polymer Composites* 46 (2025): 10619–10635, https://doi.org/10.1002/pc.29820.

40. M. Lemecha, K. Ligier, D. J. Choszcz, and M. Janulin, "Influence of Processing Temperature on Wear Properties of Materials Printed Using FDM Technology," *Tribologia* 315 (2026): 15–26, https://doi.org/10.5604/01.3001.0055.7118.

41. M. M. Y. Zaghloul, K. Steel, M. Veidt, D. Martin, M. Firouzi, and M. T. Heitzmann, "Influence of Counter-Face Grit Size and Lubricant on the Abrasive Wear Behaviour of Thermoplastic Polymers Reinforced With Glass Fibres," *Tribology Letters* 71 (2023): 102, https://doi.org/10.1007/s11249-023-01774-9.

42. F. Huang, Z. Han, M. Wei, et al., "Cryogenic Performance and Modelling of Fibre- and Nano-Reinforced Composites: Failure Mechanisms, Toughening Strategies, and Constituent-Level Behaviour," *Journal of Composites Science* 10 (2026): 36, https://doi.org/10.3390/jcs10010036.

43. D. Dubey, K. Oumghar, S. Behera, et al., "Low Cycle Fatigue Behaviour of Additively Manufactured Short Glass Fiber-Reinforced PLA Composites Subjected to Non-Symmetric Loading," *Progress in Additive*

15480569, 0, Downloaded from https://4spepublications.onlinelibrary.wiley.com/doi/10.1002/pc.71528 by Turkey Cochrane Evidence Aid, Wiley Online Library on [14/08/2026]. See the Terms and Conditions (https://onlinelibrary.wiley.com/terms-and-conditions) on Wiley Online Library for rules of use; OA articles are governed by the applicable Creative Commons License

Manufacturing 11 (2026): 2035–2058, https://doi.org/10.1007/s40964-025-01456-z.

44. X. Monnier, D. Cavallo, M. C. Righetti, et al., "Physical Aging and Glass Transition of the Rigid Amorphous Fraction in Poly(l-Lactic Acid)," *Macromolecules* 53 (2020): 8741–8750, https://doi.org/10.1021/acs.macromol.0c01182.

45. J. Benz and C. Bonten, "Rigid Amorphous Fraction as an Indicator for Polymer-Polymer Interactions in Highly Filled Plastics," *Polymers* 13 (2021): 3349, https://doi.org/10.3390/polym13193349.

46. L. Aliotta, M. Gazzano, A. Lazzeri, and M. C. Righetti, "Constrained Amorphous Interphase in Poly(l-Lactic Acid): Estimation of the Tensile Elastic Modulus," *ACS Omega* 5 (2020): 20890–20902, https://doi.org/10.1021/acsomega.0c02330.

47. R. Zhang, K. Jariyavidyanont, E. Zhuravlev, C. Schick, and R. Androsch, "Physical Aging and Glass Transition Dynamics of Semicrystalline Poly(Lactic Acid) for 3D-Printing Applications Investigated by Fast Scanning Calorimetry," *Macromolecules* 57 (2024): 32–41, https://doi.org/10.1021/acs.macromol.3c01330.

48. X. Monnier, A. Saiter, and E. Dargent, "Physical Aging in PLA Through Standard DSC and Fast Scanning Calorimetry Investigations," *Thermochimica Acta* 648 (2017): 13–22, https://doi.org/10.1016/j.tca.2016.12.006.

49. M. Colaers, W. Thielemans, and B. Goderis, "Quantitative DSC Assessment of the Polymorph-Specific Crystallinity of Poly(Lactic Acid) and the Impact of a Self-Assembling Nucleating Agent and PEG Plasticizer," *Polymers* 17 (2025): 1267, https://doi.org/10.3390/polym17091267.

Supporting Information

Additional supporting information can be found online in the Supporting Information section. **Table S1:** Analysis of variance (ANOVA) and statistical parameters for the wear depth (μm) of additively manufactured PLA and glass-fiber reinforced composites under varying sliding and aging conditions. **Figure S1:** Main effects and interactive behavior of wear-track depth (μm) for FDM-printed PLA composites, illustrating the competitive regimes between glass fiber reinforcement shielding, sliding speed variations, and environmental degradation cycles. **Table S2:** Analysis of variance (ANOVA) layout for the quantitative assessment of material composition, sliding speed, thermal cycling, and interconnected factor interactions on the wear scar width (μm) of additively manufactured parts. **Figure S2:** Main effects plots for the wear-track width (μm) of FDM-printed PLA composites, showing the shared parametric dominance of sliding speed, thermal aging duration, and material composition on lateral scar expansion. **Table S3:** General factorial regression and ANOVA results for the average coefficient of friction (COF) of FDM-printed PLA composites, highlighting the strong dominance of interconnected multi-way factor interactions on the tribological interface behavior. **Figure S3:** Main effects plots for the average coefficient of friction (COF) of FDM-printed PLA composites, illustrating the strong dominance of higher-order multi-way interactions and third-body abrasive debris evolution at the sliding interface. **Figure S4:** Unified radar comparison of the per-unit main parameter effects, highlighting the holistic degradation patterns driven by the competitive interplay between glass fiber reinforcement shielding, velocity-dependent thermal softening, and environmentally induced micro-cracking.

15480569, 0, Downloaded from https://4spepublications.onlinelibrary.wiley.com/doi/10.1002/pc.71528 by Turkey Cochrane Evidence Aid, Wiley Online Library on [14/08/2026]. See the Terms and Conditions (https://onlinelibrary.wiley.com/terms-and-conditions) on Wiley Online Library for rules of use; OA articles are governed by the applicable Creative Commons License